

# Uncertainty quantification for nanoplasmonics with adjoint-based Leja adaptive collocation and conformal maps

Niklas Georg<sup>a,b,c,\*</sup>, Dimitrios Loukrezis<sup>b,c</sup>, Ulrich Römer<sup>a</sup> and Sebastian Schöps<sup>b,c</sup>

<sup>a</sup>Institut für Dynamik und Schwingungen, Technische Universität Braunschweig, Schleinitzstraße 20, D-38106 Braunschweig, Germany

<sup>b</sup>Centre for Computational Engineering, Technische Universität Darmstadt, Dolivostraße 15, D-64293 Darmstadt, Germany

<sup>c</sup>Institut für Teilchenbeschleunigung und Elektromagnetische Felder (TEMF), Technische Universität Darmstadt, Schloßgartenstraße 8, D-64289 Darmstadt, Germany

## ARTICLE INFO

### Keywords:

adaptivity  
adjoint error indicator  
conformal maps  
hierarchical interpolation  
Maxwell's source problem  
plasmonics

## ABSTRACT

This work addresses uncertainties arising in the nano-scale fabrication of optical devices. The stochastic collocation method is used to propagate uncertainties in material and geometry to the scattering parameters of the system. A dimension-adaptive scheme based on weighted Leja nodes is employed to reduce the computational complexity. The underlying approximation spaces consist of either standard global polynomials or conformally mapped polynomials. Various numerical studies are reported, showing the benefits and drawbacks of using conformal maps for surrogate modeling. The adaptive algorithm is based on an adjoint-based error indicator, which can further be used for error correction of the (mapped) polynomial approximation. An optical grating coupler is used as a benchmark example from nano-plasmonics. For this model problem, the adaptive strategy allows us to conduct a thorough uncertainty analysis, taking into account a moderately large number of random parameters. Among various results, it is found that, interestingly, geometric sensitivities outweigh material-related sensitivities in the considered setting, even if the geometrical variations are rather small.

## 1. Introduction

Plasmonic structures offer great potential for subwavelength optics and optoelectronics [1] and have been intensively studied from both a fundamental and an application point of view in recent years. The key principle is the interaction of an optical excitation with surface plasmons on a metallic surface [2]. This interaction strongly depends on the subwavelength geometry [1], which can be suitably adjusted using modern nano-scale fabrication methods. A high coupling efficiency can be achieved, e.g. using grating couplers [3, 4, 5]. These structures can be analyzed using methods from computational electromagnetics [6], such as the rigorous coupled-wave analysis (RCWA) [7, 8], the finite-difference time-domain (FDTD) method [9, 10, 11], the boundary element method (BEM) [12, 13, 14], continuous Galerkin methods in the frequency domain [15, 16] and the discontinuous Galerkin time-domain (DGTD) method [17, 18, 19, 20, 21].

Due to recent developments in uncertainty quantification (UQ) [22], studying statistical parameter variations within the numerical simulation of fields and waves comes into reach. Quantifying uncertainties for optical components and plasmonic structures in particular is highly relevant, as relatively large variabilities of nano-scale geometrical parameters can be observed, see, e.g. [5]. In addition, in view of the complicated measurement process, uncertainties are present in dispersion parameters or the dispersion model itself. Inferring parameter statistics from measurements and assessing model-form uncertainties are important tasks of current in-

terest, but beyond the scope of this paper. Instead, we focus on the propagation of uncertainties from the model inputs to the outputs, in order to compute global probability distributions and sensitivities for physical quantities of interest (QoIs).

In the last three decades, (pseudo) spectral UQ methods have been developed as an efficient alternative to Monte Carlo simulation [22, 23, 24, 25, 26, 27]. These methods are continuously improved to address large-scale problems with many input parameters, which still pose a computational challenge nowadays. Adaptivity in combination with polynomial approximation is a promising technique to delay the curse-of-dimensionality [28, 29, 30, 31, 32]. Spectral methods have been applied in a wide range of areas for UQ purposes, e.g. fluid dynamics [33, 34] and structural mechanics [35], to mention the most common ones. Wave propagation has been considered much later and it was observed that spectral methods may fail to converge exponentially in this case [36]. In microwave engineering, polynomial approximations have been applied in [37, 38] for the case of low-dimensional uncertainty, while moderate dimensions and adaptive methods are considered in [39]. Theoretical results for the Helmholtz transmission problem as a model for acoustic scattering and nano-optics have recently been obtained in [40, 41]. In those works, analytic regularity of the solution with respect to perturbations in the scatterer geometry was obtained for large wavelengths. Based on holomorphy results, algebraic convergence rates independent of the number of random inputs were proven, thus addressing the case of infinitely many parameters.

An alternative, sometimes complementary, approach for the numerical solution of parametric problems in computational electromagnetics is model order reduction [42, 43,

\*Corresponding author: n.georg@tu-braunschweig.de

ORCID(s): 0000-0003-4394-336X (N. Georg); 0000-0003-1264-1182 (D. Loukrezis); 0000-0002-1277-7509 (U. Römer); 0000-0001-9150-0219 (S. Schöps)

[44]. Model order reduction based on moment-matching [45, 46] can be used to derive a rational parametric approximation, which is appealing in the case of reduced parametric regularity. Rational Padé-type approximations have recently been employed for a Helmholtz problem with a random wave number [47]. Moreover, in [48] a Padé-Legendre method was introduced to cope with discontinuous response surfaces, where it was also noted that high-dimensional settings are still difficult to address. In this respect, studies on rational methods are postponed to future research, although these type of methods present viable alternatives for uncertainty propagation in nano-plasmatics. If sufficiently small variations are considered, another viable alternative consists in perturbation methods, see, e.g., [49].

In this work, we propose a numerical scheme which comprises adaptive collocation, weighted Leja nodes, adjoint error techniques, and conformal maps. To the best of our knowledge, the suggested approach is a novel addition to the UQ literature. Conformal maps have been put forth in [50, 51] for the acceleration of interpolation and quadrature methods, but have not received much attention in the UQ context so far. The employed collocation scheme is dimension-adaptive [28, 29], thus being able to address the moderately high number of parameters in the considered model. In order to efficiently steer the adaptive selection of polynomials, we derive an adjoint representation of the stochastic error. Adjoint techniques have been used in a stochastic context before [52, 53], also in combination with Clenshaw-Curtis adaptive collocation [54, 55], and applied to a number of academic examples. Here, we combine adjoint techniques with hierarchical weighted Leja interpolation and conformal maps. Contrary to the works [54, 55], the use of weighted Leja nodes allows us to consider non-uniform random parameters in a straightforward manner [30, 39, 56, 57]. Our results show clearly that the use of adjoint techniques improve the efficiency of adaptive collocation, also when the more “granular” Leja points are employed.

The proposed numerical scheme is employed for UQ in a complex and technically relevant application, i.e. an optical grating coupler. We consider the optical coupling into metal-insulator-metal (MIM) plasmon modes with subwavelength diffraction gratings [5], which is illustrated in Fig. 1. A plane wave at optical frequency hits the surface of a grating coupler. The incident wave couples with a MIM plasmon mode, which propagates along the metallic surface. It is found that the MIM resonance has a significant shift (in energy) as a function of the grating depth [5] and therefore, it is of great interest to evaluate the influence of nano-technological manufacturing imperfections. Such a periodic structure can be addressed with FDTD, however, we use the finite element method (FEM) in frequency domain, as it can easily handle complex geometries. Both geometric and material parameters are modeled as random variables (RVs). Our numerical scheme is first used to derive inexpensive surrogate models, i.e. approximations of the map from the input parameters to a complex-valued QoI. Those surrogate models are then sampled to compute moments, sensitivities and confidence

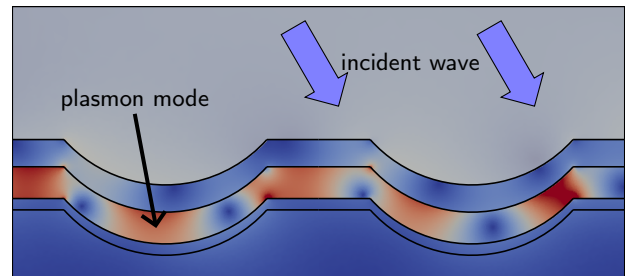


Figure 1: Optical coupling into MIM plasmon modes [5].

intervals for the QoI. Moreover, by treating the excitation frequency as an additional parameter, we use surrogate models to compute the variability of the MIM resonance. To our knowledge, this is the first exhaustive uncertainty analysis for a nano-plasmatics application. In similar physical settings, UQ studies have been conducted in the recent works [58, 59], which, however, employ numerical methods less advanced, without any adaptivity, than the one suggested in this paper. In comparison to recent theoretical studies [40, 41], we employ additional techniques for convergence acceleration and consider more complex numerical examples. We also note that, although illustrated by means of an optical grating coupler, the employed UQ methodologies apply in a much broader context.

The rest of this paper is structured as follows. In Section 2 we introduce the deterministic problem of wave scattering in periodic structures, its finite element discretization, and its parametrization. In Section 3 we present the proposed numerical UQ methods. In particular, we suggest the use of an adaptive interpolation method based on weighted Leja points and conformal maps. The adaptive algorithm is further improved by means of an adjoint error indicator, discussed in the same section. In Section 4, the suggested methods are used to conduct a UQ study for an optical grating coupler. After presenting the coupler’s numerical model and its parametrization, we first address the single-frequency case. We identify the most sensitive material and geometrical parameters and investigate the regularity of the map from the random inputs to the scattering parameter. The regularity results are based on studying the decay of the Fourier coefficients of generalized polynomial chaos (gPC) expansions, which are briefly recalled in the same section. Isotropic gPC expansions are also used for comparison purposes. Finally, we consider broadband calculations and assess the impact of material uncertainties upon the resonance frequency. In the last section we give some concluding remarks.

## 2. Maxwell’s Source Problem

In the following, we state Maxwell’s source problem for the scattering in periodic structures with excitation by an incident plane wave. We also introduce the finite element (FE) discretization for the numerical approximation of fields and scattering parameters.

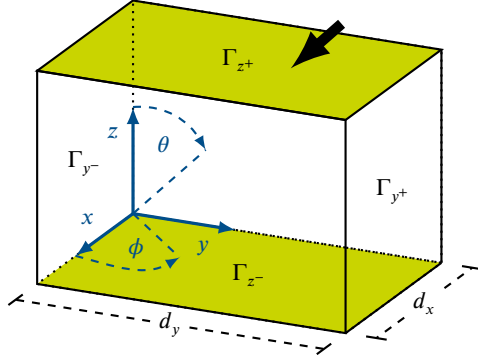


**Figure 2:** Sketch of a unit cell representing the computational domain  $D$ . The black arrow indicates the incident wavevector  $\mathbf{k}^{inc}$ .

## 2.1. Deterministic Problem

We start with the time-harmonic Maxwell's equations,

$$\nabla \times \mathbf{E} = -j\omega\mu\mathbf{H} \quad \text{in } D, \quad (1a)$$

$$\nabla \times \mathbf{H} = \mathbf{J}_s + j\omega\epsilon\mathbf{E} \quad \text{in } D, \quad (1b)$$

$$\nabla \cdot (\epsilon\mathbf{E}) = \rho \quad \text{in } D, \quad (1c)$$

$$\nabla \cdot (\mu\mathbf{H}) = 0 \quad \text{in } D, \quad (1d)$$

where  $\mathbf{E}$  denotes the electric field phasor,  $\mathbf{H}$  the magnetic field phasor,  $\mathbf{J}_s$  the source current phasor,  $\rho$  the charge density phasor,  $\omega$  the angular frequency,  $\epsilon$  the dispersive complex-valued permittivity,  $\mu$  the permeability and  $D$  the computational domain to be specified. The permeability  $\mu = \mu_r\mu_0$ , where  $\mu_r$  and  $\mu_0$  represent the relative and vacuum permeability, respectively, is assumed to be nondispersive. In absence of charges and source currents, i.e.  $\rho = 0$  and  $\mathbf{J}_s = 0$ , the so-called curl-curl equation reads

$$\nabla \times (\mu_r^{-1}\nabla \times \mathbf{E}) - \omega^2\epsilon\mu_0\mathbf{E} = 0 \quad \text{in } D, \quad (2)$$

to be endowed with appropriate boundary conditions.

Given an infinitely periodic structure and a periodic excitation, the computational domain  $D$  can be confined to a single unit cell of the periodic structure, based on Floquet's Theorem [15, Chapter 13]. The unit cell is illustrated in Fig. 2. Without loss of generality we assume periodicity in the  $x$  and  $y$  directions, whereas  $\Gamma_{z+}$  and  $\Gamma_{z-}$  denote the boundaries in the non-periodic direction. At  $\Gamma_{z+}$  the structure is excited by an incident plane wave

$$\mathbf{E}^{inc} = \mathbf{E}_0 e^{-j\mathbf{k}^{inc} \cdot \mathbf{r}}, \quad (3)$$

$$\mathbf{k}^{inc} = \begin{bmatrix} k_x^{inc} \\ k_y^{inc} \\ k_z^{inc} \end{bmatrix} = -k_0 \begin{bmatrix} \sin \theta^{inc} \cos \phi^{inc} \\ \sin \theta^{inc} \sin \phi^{inc} \\ \cos \theta^{inc} \end{bmatrix}, \quad (4)$$

where  $\theta^{inc}$ ,  $\phi^{inc}$  are the angles of incidence and  $k_0 = \omega/\sqrt{\mu_0\epsilon_0}$  the wavenumber in vacuum. It is worth noting that, due to the oblique angles, the periodicity of the excitation differs from the geometrical periodicity of the structure. According to Floquet's theorem, we need to enforce periodic phase-shift boundary conditions on  $\Gamma_{x+} \cup \Gamma_{x-}$  and on  $\Gamma_{y+} \cup \Gamma_{y-}$ , i.e.

$$\mathbf{E}|_{\Gamma_{x+}} = \mathbf{E}|_{\Gamma_{x-}} e^{j\psi_x}, \quad \psi_x = -k_x^{inc} d_x \quad (5a)$$

$$\mathbf{E}|_{\Gamma_{y+}} = \mathbf{E}|_{\Gamma_{y-}} e^{j\psi_y}, \quad \psi_y = -k_y^{inc} d_y \quad (5b)$$

where the phase-shifts  $\psi_x$ ,  $\psi_y$  depend only on the wavevector  $\mathbf{k}^{inc}$  of the incident wave at  $\Gamma_{z+}$  and on the dimensions  $d_x$ ,  $d_y$  of the unit cell.

To truncate the structure in the non-periodic direction at  $\Gamma_{z+}$ , we employ a Floquet absorbing boundary condition [15] as derived in Appendix A. At  $\Gamma_{z-}$ , a perfect electric conductor (PEC) boundary condition is applied to truncate the structure, however, different boundary conditions are also possible, e.g. again a Floquet absorbing boundary condition or perfectly matched layers (PML) [15]. In summary, we are concerned with the boundary value problem

$$\nabla \times (\mu_r^{-1}\nabla \times \mathbf{E}) - \omega^2\epsilon\mu_0\mathbf{E} = 0 \quad \text{in } D, \quad (6a)$$

$$\mathbf{E}|_{\Gamma_{x+}} e^{-j\psi_x} = \mathbf{E}|_{\Gamma_{x-}} \quad \text{on } \Gamma_{x+} \cup \Gamma_{x-}, \quad (6b)$$

$$\mathbf{E}|_{\Gamma_{y+}} e^{-j\psi_y} = \mathbf{E}|_{\Gamma_{y-}} \quad \text{on } \Gamma_{y+} \cup \Gamma_{y-}, \quad (6c)$$

$$\mathbf{n} \times \mathbf{E} = 0 \quad \text{on } \Gamma_{z-}, \quad (6d)$$

$$\mathbf{n} \times \mathbf{H} + \mathcal{G}(\mathbf{E}) = \mathcal{F}^{inc} \quad \text{on } \Gamma_{z+}, \quad (6e)$$

where  $\mathcal{G}(\mathbf{E})$  and  $\mathcal{F}^{inc}$  are derived and defined in Appendix A, see (111)-(113).

### 2.1.1. Weak formulation and discretization

To simplify the notation, we introduce the traces

$$\mathbf{u}_T := (\mathbf{n}_\Gamma \times \mathbf{u}|_\Gamma) \times \mathbf{n}_\Gamma, \quad (7a)$$

$$\mathbf{u}_t := \mathbf{n}_\Gamma \times \mathbf{u}|_\Gamma, \quad (7b)$$

where  $\Gamma := \partial D$  denotes the boundary of  $D$  and  $\mathbf{n}_\Gamma$  refers to its outer unit normal. Note that the trace operators are denoted by subscripts, for brevity of notation.

By building the inner product of (6a) with tests function  $\mathbf{E}' \in V$ , where  $V$  is to be determined, and integration by parts we obtain

$$\begin{aligned} (\mu_r^{-1}\nabla \times \mathbf{E}, \nabla \times \mathbf{E}')_D - \omega^2\mu_0 (\epsilon\mathbf{E}, \mathbf{E}')_D \\ - j\omega\mu_0 (\mathbf{H}_t, \mathbf{E}'_T)_\Gamma = 0. \end{aligned} \quad (8)$$

The boundary integral can be further simplified, i.e. the contributions on  $\Gamma_{x+}$ ,  $\Gamma_{x-}$  and  $\Gamma_{y+}$ ,  $\Gamma_{y-}$  cancel each other due to the periodic phase-shift boundary conditions (6b), (6c) of trial and test functions. We further eliminate the portion of the integral on  $\Gamma_{z-}$  by demanding that the test functions  $\mathbf{E}'$  fulfill the PEC boundary condition (6d).

The appropriate function space  $V$  for a weak formulation is a subspace of  $\mathbf{H}(\text{curl}; D)$ , i.e. the (complex) vector function space of square-integrable functions with square-integrable curl. For more details on function spaces in the context of Maxwell's source problem, the reader is referred to [16, Chapter 3]. To account for the boundary conditions in (6), the function space is chosen as

$$\begin{aligned} V := \{ \mathbf{v} \in \mathbf{H}(\text{curl}; D) : \mathbf{v}_T|_{\Gamma_{z-}} = 0 \\ \wedge \mathbf{v}_T|_{\Gamma_{x+}} = -\mathbf{v}_T|_{\Gamma_{x-}} e^{j\psi_x} \\ \wedge \mathbf{v}_T|_{\Gamma_{y+}} = -\mathbf{v}_T|_{\Gamma_{y-}} e^{j\psi_y} \\ \wedge \mathbf{v}_T|_{\Gamma_{z+}} \in (L^2(\Gamma_{z+}))^3 \}, \end{aligned} \quad (9)$$

where the condition  $\mathbf{v}_T|_{\Gamma_{z^+}} \in (L^2(\Gamma_{z^+}))^3$  is required to obtain a well-defined boundary integral. Employing the Floquet absorbing boundary condition (6e) on  $\Gamma_{z^+}$  yields the weak formulation: find  $\mathbf{E} \in V$  s.t.

$$\begin{aligned} & (\mu_r^{-1} \nabla \times \mathbf{E}, \nabla \times \mathbf{E}')_D - \omega^2 \mu_0 (\epsilon \mathbf{E}, \mathbf{E}')_D \\ & + j\omega \mu_0 (\mathcal{G}(\mathbf{E}), \mathbf{E}'_{\Gamma})_{\Gamma_{z^+}} = j\omega \mu_0 (\mathbf{F}^{\text{inc}}, \mathbf{E}'_{\Gamma})_{\Gamma_{z^+}} \quad (10) \\ & \quad \forall \mathbf{E}' \in V, \end{aligned}$$

To ensure a curl-conforming discretization of (10), we approximate the electric field  $\mathbf{E}$  numerically as

$$\mathbf{E}_h(\mathbf{x}) = \sum_{j=1}^{N_h} c_j \mathbf{N}_j(\mathbf{x}) \quad (11)$$

where  $\mathbf{N}_j$  denotes Nédélec basis functions of the first kind [60, 16] and 1st or 2nd order, defined on a tetrahedral mesh of the domain  $D$ . Further details on the discretization are given in Appendix B.

In practice, one is often interested in reflection and transmission coefficients, in addition to the field solution  $\mathbf{E}$  itself. Therefore, we define the (complex-valued) scattering parameters as (affine-) linear functionals of  $\mathbf{E}$

$$S_{\alpha,mn} := (\mathbf{E}_T - \mathbf{E}_T^{\text{inc}}, \pi_T [\mathbf{E}_{\alpha,mn}])_{\Gamma_{z^+}}, \quad (12)$$

where  $\alpha \in \{\text{TE, TM}\}$ ,  $m \in \mathbb{Z}$ ,  $n \in \mathbb{Z}$  and  $\mathbf{E}_{\alpha,mn}$  are Floquet modes defined in Appendix A.

## 2.2. Parametrized model

In this subsection we specify the material distribution of the complex permittivity  $\epsilon$ . In particular, we assume a linear material behaviour for  $\epsilon$  and  $\mu$  inside  $D$ . Let the domain  $D$  be composed of  $M$  non-overlapping subdomains  $D_m$ , i.e.  $\overline{D} = \bigcup_{m=1}^M \overline{D_m}$ . We further assume that the dispersive permittivity  $\epsilon(\mathbf{x}, \omega)$  is spatially piecewise constant on each subdomain  $D_m$  and depends smoothly on a given vector of  $N$  parameters  $\mathbf{y} \in \Xi \subset \mathbb{R}^N$

$$\begin{aligned} \epsilon(\mathbf{x}, \omega, \mathbf{y}) &= \sum_{m=1}^M \epsilon_m(\omega, \mathbf{y}) \mathbb{1}_m(\mathbf{x}, \mathbf{y}), \\ \text{where } \mathbb{1}_m(\mathbf{x}, \mathbf{y}) &= \begin{cases} 1, & \mathbf{x} \in D_m(\mathbf{y}), \\ 0, & \mathbf{x} \notin D_m(\mathbf{y}). \end{cases} \quad (13) \end{aligned}$$

On the one hand, the parameter vector  $\mathbf{y}$  can be used to represent variations in the material parameters, e.g. different permittivities, refractive indices or extinction coefficients, by changing the coefficients  $\epsilon_m(\omega, \mathbf{y})$ . On the other hand, it also represents geometric variations of the structure inside the unit cell, since the subdomains  $D_m(\mathbf{y})$  for each material depend on  $\mathbf{y}$  as well.

The parametrized weak formulation reads: find  $\mathbf{E}(\mathbf{y}) \in V$  s.t.

$$a_{\mathbf{y}}(\mathbf{E}(\mathbf{y}), \mathbf{E}') = l(\mathbf{E}') \quad \forall \mathbf{E}' \in V, \quad (14)$$

where

$$\begin{aligned} a_{\mathbf{y}}(\mathbf{E}, \mathbf{E}') &:= (\mu_r^{-1} \nabla \times \mathbf{E}(\mathbf{y}), \nabla \times \mathbf{E}')_D \\ & - \omega^2 \mu_0 (\epsilon(\mathbf{y}) \mathbf{E}(\mathbf{y}), \mathbf{E}')_D \\ & + j\omega \mu_0 (\mathcal{G}(\mathbf{E}(\mathbf{y})), \mathbf{E}'_{\Gamma})_{\Gamma_{z^+}}. \end{aligned} \quad (15)$$

The parameter-dependent scattering parameters are given as

$$S_{\alpha,mn}(\mathbf{y}) = (\mathbf{E}_T(\mathbf{y}) - \mathbf{E}_T^{\text{inc}}, \pi_T [\mathbf{E}_{\alpha,mn}])_{\Gamma_{z^+}}, \quad (16)$$

where  $\alpha \in \{\text{TE, TM}\}$ .

## 3. Uncertainty Quantification

In this section, we consider the general problem of finding

$$\mathbf{u}(\mathbf{y}) \in \tilde{V} \text{ s.t. } \tilde{a}_{\mathbf{y}}(\mathbf{u}(\mathbf{y}), \mathbf{v}) = \tilde{l}_{\mathbf{y}}(\mathbf{v}) \quad \forall \mathbf{v} \in \tilde{V}, \quad (17)$$

where  $\tilde{V}$  denotes a suitable Hilbert space. Problem (17) may represent the model of Section 2.2, or other parametrized differential equations with a continuous sesquilinear form  $\tilde{a}_{\mathbf{y}}(\cdot, \cdot)$  and a continuous (anti)linear form  $\tilde{l}_{\mathbf{y}}(\cdot)$ . We assume the map  $\mathbf{u} : \Xi \rightarrow \tilde{V}$  to be well-defined and sufficiently smooth. We are interested in the model's response which may be the solution  $\mathbf{u}(\mathbf{y})$  itself or a functional  $J_{\mathbf{y}}(\mathbf{u}(\mathbf{y}))$ , e.g. a scattering parameter, commonly referred to as the QoI. In this work, we focus on single-valued and complex QoIs, i.e.  $J_{\mathbf{y}}(\mathbf{u}(\mathbf{y})) \in \mathbb{C}$ . For brevity of notation and owing to the well-posedness of the system, we shall replace  $J_{\mathbf{y}}(\mathbf{u}(\mathbf{y}))$  with  $J(\mathbf{y})$ , where  $J$  can be understood as an abstract representation of the map from the input parameters to the QoI.

We now assume that the input parameters are given as independent RVs  $Y_n$ ,  $n = 1, 2, \dots, N$ . We introduce the random vector  $\mathbf{Y} = (Y_1, Y_2, \dots, Y_N)^\top$ , defined on the probability space  $(\Theta, \Sigma, P)$ , where  $\Theta$  denotes the sample space,  $\Sigma$  the sigma-algebra of events and  $P$  the probability measure, its image set  $\Xi = \Xi_1 \times \Xi_2 \dots \times \Xi_N \subset \mathbb{R}^N$  and its probability density function (PDF)  $\varphi(\mathbf{y}) = \prod_{n=1}^N \varphi_n(y_n)$ , such that  $\mathbf{Y} : \Theta \rightarrow \Xi$  and  $\varphi : \Xi \rightarrow \mathbb{R}_+$ . Then, the parameter vector represents a realization of the random vector, i.e.  $\mathbf{y} = \mathbf{Y}(\theta) \in \Xi$ ,  $\theta \in \Theta$ . Assuming independence is necessary for the tensor-product constructions in the collocation method, however, dependence could also be taken into account through a suitable transformation, for instance, Rosenblatt or Nataf transformations [61, 62]. In view of this transformation, we assume in this section that the image set  $\Xi$  is given as the hypercube  $[-1, 1]^N$ , for simplicity.

Now, the QoI is itself a RV and we are interested in quantifying uncertainty, e.g. by computing its moments, PDF, quantiles, etc. In the case where the QoI is smooth (ideally, analytic) with respect to the input RVs, spectral UQ methods [33, 63] may be employed. Then,  $J$  is particularly well suited to be approximated by polynomials such that

$$J(\mathbf{y}) \approx \tilde{J}(\mathbf{y}) = \sum_{m=0}^M s_m \Psi_m(\mathbf{y}), \quad (18)$$

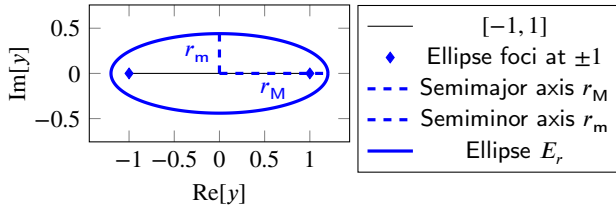


Figure 3: Bernstein ellipse  $E_r$  of size  $r = r_M + r_m$ .

where  $\Psi_m : \Xi \rightarrow \mathbb{R}$  are multivariate polynomials and  $s_m \in \mathbb{C}$  the associated coefficients, and fast convergence can be expected. Once an approximation in the form of (18) is available, it can be used as an inexpensive substitute of the original computational model for sampling-based computations. Alternatively, some statistical information regarding the QoI can be derived directly from the coefficients. In the context of the present work, we will use approximations in the form of (18), based either on gPC [64, 65, 66, 67, 26] or on sparse grid interpolation [25, 68, 69, 28, 70, 30, 71, 55, 27], both of which can be combined with a conformal mapping.

### 3.1. Univariate interpolation and conformal maps

We first discuss univariate interpolation in some detail, since it is also the key building block for the tensor product constructions used in the multivariate case. In particular, we consider the univariate function  $f : [-1, 1] \rightarrow \mathbb{C}$ ,

$$f(y) := J(y, 0, \dots, 0). \quad (19)$$

Note that the position of the variable argument  $y$  is arbitrary in the above expression.

Let's assume that  $f$  is analytic on  $[-1, 1]$  and can be analytically extended onto  $E_r$ , where  $E_r$  refers to an open Bernstein ellipse of size  $r$ , i.e. an ellipse in the complex plane with foci at  $\pm 1$  and semi-minor and semi-major axis summing up to  $r$ , as illustrated in Fig. 3. Then, cf. [51, Theorem 8.2], the error of the univariate polynomial best approximation  $f_M^*$  of degree  $M$  can be estimated as

$$\|f - f_M^*\|_\infty \leq \frac{C_B r^{-M}}{r - 1}, \quad (20)$$

where  $\|\cdot\|_\infty$  denotes the supremum-norm on  $[-1, 1]$  and the positive constant  $C_B > 0$  depends on the uniform bound of the analytic continuation of  $f$  in  $E_r$ . We consider a polynomial interpolant

$$f_M(y) := \sum_{i=0}^M f(y^{(i)}) l_i(y), \quad (21)$$

where  $\{l_i\}_{i=0}^M$  and  $\{y^{(i)}\}_{i=0}^M$  denote univariate Lagrange polynomials and a set of distinct nodes, respectively. There holds

$$\begin{aligned} \|f - f_M\|_\infty &\leq (1 + \Delta_M) \|f - f_M^*\|_\infty \\ &\leq (1 + \Delta_M) \frac{C_B r^{-M}}{r - 1}, \end{aligned} \quad (22)$$

where

$$\Delta_M := \max_{y \in [-1, 1]} \sum_{i=0}^M |l_i(y)| \quad (23)$$

denotes the Lebesgue constant. If  $\Delta_M$  grows sub-exponentially, the polynomial interpolation converges uniformly (for analytic functions). However, the convergence rate depends on the regularity of the analytic continuation of  $f$  in the complex plane. This is illustrated by considering the Runge function

$$f_R(y; c) = \frac{1}{1 + cy^2}, \quad c \in \mathbb{R}^+, y \in [-1, 1], \quad (24)$$

which is illustrated in Fig. 4a, as a benchmark example. This function is analytic on  $[-1, 1]$  but the analytic continuation has a complex conjugate pole pair at  $y = \pm i \frac{1}{\sqrt{c}}$ , limiting the size of the largest Bernstein ellipse where the function  $f_R$  is analytic. Fig. 4b demonstrates the effect on the convergence rate, where for increasing constants  $c$ , corresponding to a reduced size of the region of analyticity, a reduced convergence rate can be observed. The plot shows the convergence of the polynomial interpolant associated to unweighted Leja points in the empirical supremum-norm with a cross-validation sample of size 1000.

Hale and Trefethen [72] have raised and discussed the question *whether polynomial methods are an optimal choice for functions analytic in an  $\epsilon$ -neighborhood*, in the context of numerical quadrature. Such a neighborhood is depicted in Fig. 5 together with the largest Bernstein ellipse contained in its interior. They have pointed out that, in this case, superior methods to Gauss quadrature can be derived by conformally mapping the Bernstein ellipse  $E_r$  to a *straighter* region  $\Omega_r = g(E_r)$ , as illustrated in Fig. 6. As will be discussed in the following, this approach is also beneficial for (polynomial) interpolation. In accordance with [72], we focus in this work on conformal mappings  $g : E_r \rightarrow \Omega_r$  which map the unit interval to itself, i.e.

$$g([-1, 1]) = [-1, 1], \quad (25)$$

and also fulfill

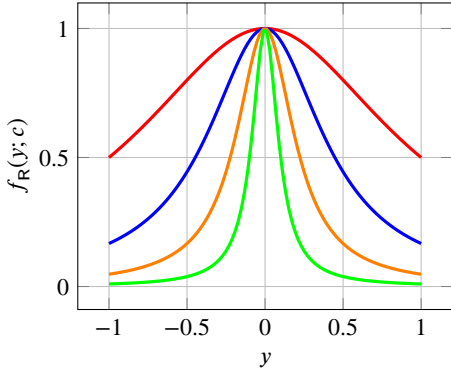
$$g(\pm 1) = \pm 1. \quad (26)$$

This ensures that the transplanted interpolation nodes

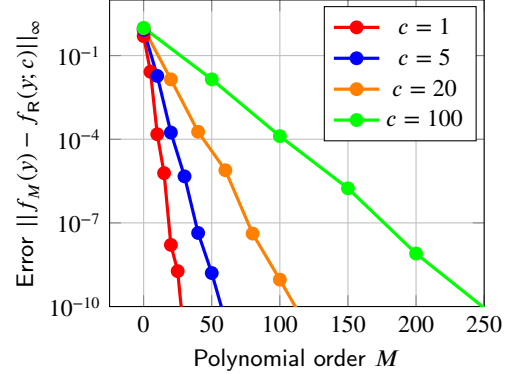
$$\{\hat{y}^{(i)}\}_{i=0}^M := \{g(y^{(i)})\}_{i=0}^M \quad (27)$$

are still real numbers contained in the considered image set  $\Xi_n$ . There are various choices for  $g$ , see e.g. [73], however, in this work we focus on the *sausage mapping* proposed in [72]. It is defined by a  $d$ -th order Maclaurin expansion of the inverse sin function which is then normalized such that (26) is fulfilled:

$$g_S(y; d) = \left( \sum_{i=0}^d \frac{2}{4^i (2i+1)i!} \right)^{-1} \sum_{i=0}^d \frac{2y^{2i+1}}{4^i (2i+1)i!}. \quad (28)$$



(a) Runge function  $f_R(y; c)$  for different  $c \in \mathbb{R}^+$  and  $y \in [-1, 1]$ .



(b) Geometric convergence rates of Leja interpolants.

Figure 4: Runge function and convergence of polynomial approximations.

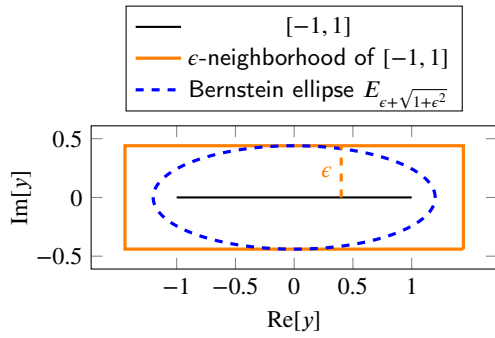


Figure 5:  $\epsilon$ -neighborhood and largest interior Bernstein ellipse.

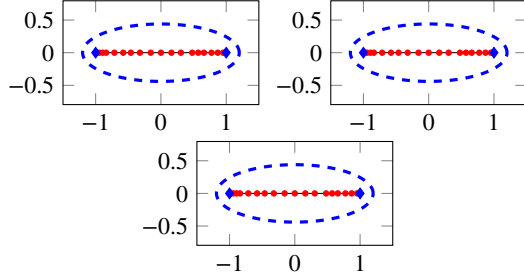


Figure 6: Conformal map of a Bernstein ellipse.

An alternative mapping, due to Kosloff and Tal-Ezer [74], is given by

$$g_{KTE}(y; \alpha) = \frac{\arcsin(\alpha y)}{\arcsin \alpha}, \quad \alpha \in (0, 1). \quad (29)$$

It can be observed that the transplanted nodes are more evenly distributed, see Fig. 7.

We interpolate the transplanted knots  $\{\hat{y}^{(i)}\}$  using mapped Lagrange polynomials  $\hat{l}_i = l_i \circ g^{-1}$ , shown in Fig. 8a. Obviously, the mapped Lagrange polynomials also have the property

$$\hat{l}_j(\hat{y}^{(i)}) = l_j \circ g^{-1}(\hat{y}^{(i)}) = l_j(y^{(i)}) = \delta_{ij}, \quad (30)$$

where  $\delta_{ij}$  denotes the Kronecker delta. Thus, the mapped

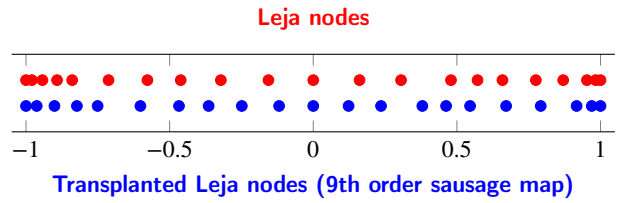


Figure 7: Leja and transplanted Leja interpolation nodes.

interpolant  $\hat{f}_M$  is defined by

$$\hat{f}_M(y) = \sum_{i=0}^M f(\hat{y}^{(i)}) \hat{l}_i(y). \quad (31)$$

To derive an error bound for the transplanted interpolation, we first introduce the function  $h := f \circ g$ . We assume that  $h$  can be continued analytically to  $E_{\hat{r}}$ , where it is uniformly bounded. Let  $h_M$  be the  $M$ -th order polynomial interpolant of  $h$  on the original nodes  $\{y^{(i)}\}_{i=0}^M$ . We observe that the mapped interpolant  $\hat{f}_M$  is equivalent to  $h_M \circ g^{-1}$  as

$$\hat{f}_M = \sum_{i=0}^M f(g(y^{(i)})) l_i \circ g^{-1} = h_M \circ g^{-1}. \quad (32)$$

Due to (25), we obtain

$$\|f - \hat{f}_M\|_\infty = \|(f - \hat{f}_M) \circ g \circ g^{-1}\|_\infty \quad (33)$$

$$= \|(h - h_M) \circ g^{-1}\|_\infty \quad (34)$$

$$= \|h - h_M\|_\infty \quad (35)$$

$$\leq (1 + \Delta_M) \|h - h_M^*\|_\infty \quad (36)$$

$$\leq (1 + \Delta_M) \frac{\hat{C}_B \hat{r}^{-M}}{\hat{r} - 1}. \quad (37)$$

The convergence rate is improved if  $\hat{r} > r$ , which we confirm numerically in Fig. 8b, where the 9-th order sausage map  $g_S(y; 9)$  is employed. Since  $g_S(y; 9)^{-1}$  is not known analytically, we approximate the inverse mapping by a Chebyshev approximation of order 100 (up to machine precision).

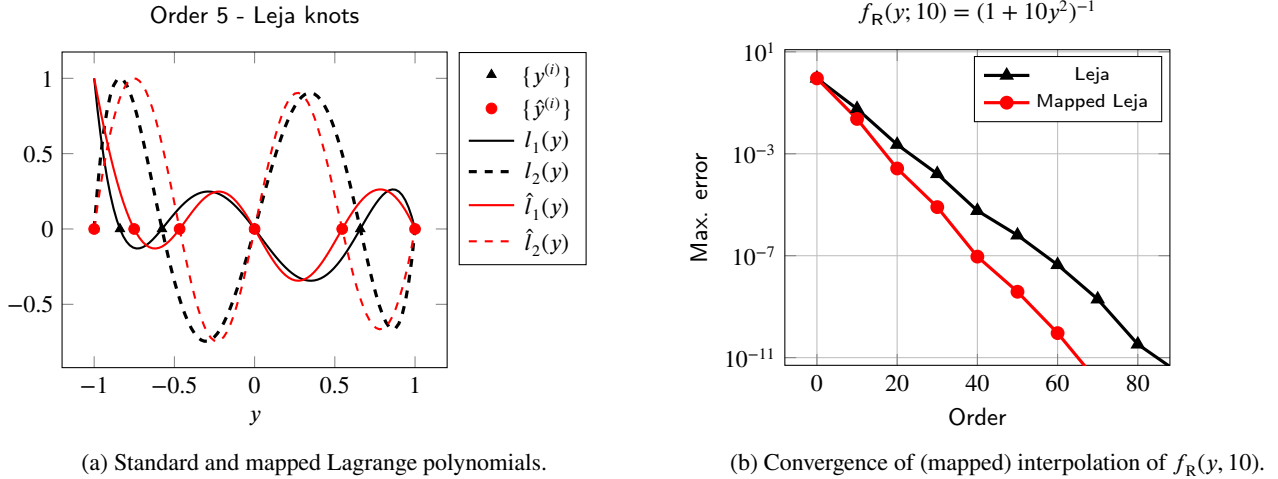


**Figure 8:** Mapped Leja interpolation polynomials and numerical orders for increasing polynomial degrees.

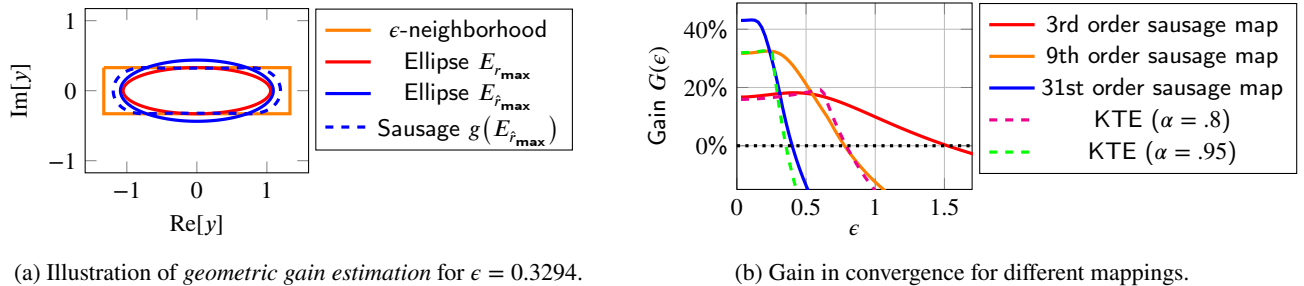


**Figure 9:** Convergence gain  $G$  by employing mapped approximations.

If the region of analyticity is known, one can estimate the gain of employing a conformal mapping a priori (based on the convergence estimates), as illustrated in Fig. 9a. Let the size of the largest Bernstein ellipse in the region of analyticity be  $r_{\max}$  and the size of the largest Bernstein ellipse, which is fully mapped into this region be  $\hat{r}_{\max}$ . The convergence gain is then given by

$$G = \frac{\log \hat{r}_{\max}}{\log r_{\max}} - 1. \quad (38)$$

We evaluate the gain  $G$  for functions which are analytic in  $\epsilon$ -neighborhoods of  $[-1, 1]$ , see Fig. 9b, by numerically computing  $\hat{r}_{\max}$  for different mappings. It should be noted that higher gains can be expected, if mappings would be employed, which are specifically tailored to the positions of the poles in the complex plane. However, usually the exact position of these poles is not known a priori and this approach is therefore not pursued any further. The interested reader is referred to [73]. In the remaining part of the paper, we work with the 9-th order sausage mapping  $g_S(y; 9)$  since a detailed comparison of different mappings is not in the scope of the present paper. The particular mapping is selected because it has already been established in [72, 73] and Fig. 9b confirms a significant gain in convergence for a substantial range of  $\epsilon$ -neighborhoods. Additionally, in contrast to the map (29), it does not introduce an artificial singularity.

### 3.2. Sparse grid interpolation

Approximations based on sparse grid interpolation are commonly referred to as sparse grid stochastic collocation methods [25, 71, 27]. Those methods are based on combinations of univariate interpolation rules, defined by an interpolation level  $\ell_n \in \mathbb{N}_0$ , a monotonically increasing level-to-nodes function  $m_n : \mathbb{N}_0 \rightarrow \mathbb{N}$ , where  $m_n(\ell_n) =: m_{\ell_n}$  and  $m_n(0) = 1$  and a grid of  $m_{\ell_n}$  (mapped) interpolation nodes

$$Z_{\ell_n} = \left\{ \hat{y}_n^{(i_n)} \right\}_{i_n=0}^{m_{\ell_n}-1}. \quad (39)$$

Introducing the multi-index  $\boldsymbol{\ell} = (\ell_1, \ell_2, \dots, \ell_N) \in \mathbb{N}_0^N$ , the tensor-product multivariate approximation is obtained as

$$J(\mathbf{y}) \approx \tilde{J}(\mathbf{y}) = \sum_{\mathbf{i}: \hat{\mathbf{y}}^{(\mathbf{i})} \in Z_{\boldsymbol{\ell}}} J(\hat{\mathbf{y}}^{(\mathbf{i})}) \hat{L}_{\boldsymbol{\ell}, \mathbf{i}}(\mathbf{y}), \quad (40)$$

where  $\hat{\mathbf{y}}^{(\mathbf{i})} = (\hat{y}_1^{(i_1)}, \hat{y}_2^{(i_2)}, \dots, \hat{y}_N^{(i_N)}) \in Z_{\boldsymbol{\ell}}$  are multivariate interpolation nodes, uniquely identified by the multi-index  $\mathbf{i} = (i_1, i_2, \dots, i_N) \in \mathbb{N}_0^N$  and  $Z_{\boldsymbol{\ell}} = Z_{\ell_1} \times Z_{\ell_2} \times \dots \times Z_{\ell_N}$  is the tensor grid of interpolation nodes.

Moreover,  $\hat{L}_{\boldsymbol{\ell}, \mathbf{i}}$  are mapped multivariate Lagrange polynomials, obtained by the concatenation  $\hat{L}_{\boldsymbol{\ell}, \mathbf{i}} = L_{\boldsymbol{\ell}, \mathbf{i}} \mathbf{g}^{-1}$

with

$$L_{\ell,i}(\mathbf{y}) = \prod_{n=1}^N l_{\ell_n, i_n}(y_n), \quad (41)$$

where

$$l_{\ell_n, i_n}(y_n) := \begin{cases} \prod_{k=1, k \neq i_n}^{m_{\ell_n}} \frac{y_n - y_n^{(k)}}{y_n^{(i_n)} - y_n^{(k)}}, & \ell_n \neq 0, \\ 1, & \ell_n = 0. \end{cases} \quad (42)$$

Obviously, for the trivial conformal mapping  $\mathbf{g} : \mathbf{y} \mapsto \mathbf{y}$ , it holds  $\hat{L}_{\ell,i} = L_{\ell,i}$ . More details on the multivariate conformal mapping  $\mathbf{g}$  will be given below. It should be noted that (41) is used for the ease of exposition, in the actual implementation the barycentric representation is used [75]. Since  $J(\mathbf{y})$  has to be evaluated for each  $\mathbf{y}^{(i)} \in Z_{\ell}$ , the complexity of the tensor-product approach is  $\mathcal{O}(m_k^N)$ , where

$$m_k := \max_n m_{\ell_n}. \quad (43)$$

This complexity can be mitigated to  $\mathcal{O}\left(m_k (\log m_k)^{N-1}\right)$  without compromising the approximation's accuracy by employing Smolyak sparse grids [76]. We introduce the approximation level  $k \in \mathbb{N}_0$  and define the multi-index set  $\Lambda_k$ , such that

$$\Lambda_k := \{\ell : |\ell| = \ell_1 + \ell_2 + \dots + \ell_N \leq k\}. \quad (44)$$

Then, the sparse grid of multivariate interpolation nodes  $Z_{\Lambda_k}$  is constructed as

$$Z_{\Lambda_k} = \bigcup_{k-N+1 \leq |\ell| \leq k} Z_{\ell}, \quad (45)$$

and the interpolation is given by

$$\mathcal{I}_{\Lambda_k}[J](\mathbf{y}) = \sum_{\mathbf{i} : \hat{\mathbf{y}}^{(i)} \in Z_{\Lambda_k}} J(\hat{\mathbf{y}}^{(i)}) \hat{L}_{\ell,i}(\mathbf{y}). \quad (46)$$

### 3.2.1. Mapped Leja nodes, hierarchical interpolation and adaptivity

As shown in [68], Smolyak formulas are in general not interpolatory, unless based on nested sequences of univariate interpolation nodes, such that  $Z_{\ell_{n-1}} \subset Z_{\ell_n}$ . Moreover, to ensure accuracy and fast convergence of the approximation, the interpolation nodes should be chosen in agreement with the PDFs  $\varrho_n(y_n)$ . We opt for weighted Leja interpolation nodes, as in [30]. Omitting conformal mappings for the moment, we consider a univariate, continuous and positive weight function. Here, this weight function is given by a univariate PDF  $\varrho_n(y_n)$ ,  $\varrho_n : \Xi_n \rightarrow \mathbb{R}_+$ . A sequence of univariate Leja nodes  $y_n^{(k)} \in \Xi_n$ ,  $k = 0, 1, 2, \dots$ , can be constructed by solving the optimization problem

$$y_n^{(K)} = \arg \min_{y_n \in \Xi_n} \sqrt{\varrho_n(y_n)} \prod_{k=0}^{K-1} |y_n - y_n^{(k)}|, \quad (47)$$

where the starting node  $y_n^{(0)}$  is arbitrarily chosen. For further details on the construction of weighted Leja nodes and an analysis of their properties, see [30]. We justify the choice of Leja nodes as follows. First of all, Leja nodes satisfy the nestedness requirement by construction. Secondly, they allow complete freedom in the choice of the level-to-nodes function  $m_n(\ell_n)$ . Finally, they can be tailored to any given PDF. In comparison, the commonly employed Clenshaw-Curtis nodes would restrict us to the rapidly growing level-to-nodes function  $m_n(\ell_n) = 2^{\ell_n} + 1$ . In the following, we employ the level-to-nodes function  $m_n(\ell_n) = \ell_n + 1$ ,  $\ell_n \in \mathbb{N}_0$ , and denote with  $y_n^{(\ell_n)}$  the single extra node corresponding to interpolation level  $\ell_n$ , i.e.  $y_n^{(\ell_n)} = Z_{\ell_n} \setminus Z_{\ell_n-1}$ . We also introduce for each parameter a conformal map  $g_n$ , as discussed in Section 3.1. Then, the mapped univariate Leja nodes  $\hat{y}_n^{(k)}$  are obtained as  $\hat{y}_n^{(k)} = g_n(y_n^{(k)})$ . Of course, for the trivial map  $g_n : y_n \mapsto y_n$  we recover the original Leja nodes  $\hat{y}_n^{(k)} = y_n^{(k)}$ . The multivariate conformal mapping is then obtain by a tensor product construction as

$$\mathbf{g}(\mathbf{y}) = g_1(y_1) \cdots g_N(y_N). \quad (48)$$

In the multivariate case, nested grids of multivariate interpolation nodes can be constructed by enforcing the use of downward-closed (also, monotone or lower) multi-index sets [28, 29]. Such sets are known to preserve the telescopic properties of the series in (46) [29]. Moreover, sequences of nested, downward-closed multi-index sets result in polynomial approximations of increasing accuracy [28]. Given a multi-index set  $\Lambda$ , let us first define its forward and backward neighbor multi-index sets,  $\Lambda_+$  and  $\Lambda_-$ , respectively, such that

$$\Lambda_+ := \{\ell + \mathbf{e}_n, \forall \ell \in \Lambda, \forall n = 1, \dots, N\}, \quad (49a)$$

$$\Lambda_- := \{\ell - \mathbf{e}_n, \forall \ell \in \Lambda, \forall n = 1, \dots, N : \ell_n > 0\}, \quad (49b)$$

where  $\mathbf{e}_n$  is the  $n$ -th unit vector. Then,  $\Lambda$  is said to be downward-closed if and only if

$$\Lambda_- \subset \Lambda. \quad (50)$$

Assuming now a multi-index  $\ell \notin \Lambda$  such that  $\Lambda \cup \ell$  is downward-closed, it holds that  $Z_{\Lambda} \subset Z_{\Lambda \cup \ell}$  and

$$\hat{\mathbf{y}}^{(\ell)} = Z_{\Lambda \cup \ell} \setminus Z_{\Lambda}. \quad (51)$$

Then, (46) can be naturally transformed into the hierarchical interpolation

$$\mathcal{I}_{\Lambda \cup \ell}[J](\mathbf{y}) = \mathcal{I}_{\Lambda}[J](\mathbf{y}) + s_{\ell} \hat{H}_{\ell}(\mathbf{y}), \quad (52)$$

where the coefficients  $s_{\ell} \in \mathbb{C}$ , known as “hierarchical surpluses”, are given by

$$s_{\ell} = J(\hat{\mathbf{y}}^{(\ell)}) - \mathcal{I}_{\Lambda}[J](\hat{\mathbf{y}}^{(\ell)}), \quad (53)$$

and  $\hat{H}_{\ell}$  are multivariate mapped hierarchical polynomials, defined as

$$\hat{H}_{\ell}(\mathbf{y}) = \prod_{n=1}^N \hat{h}_{\ell_n}(y_n), \quad (54)$$

**Data:** QoI  $J(\mathbf{y})$ , conformal map  $\mathbf{g}$ , multi-index set  $\Lambda$ , budget  $B$   
**Result:** sparse grid  $Z_{\Lambda \cup \Lambda_+^{\text{adm}}}$ , approximation  $\mathcal{I}_{\Lambda \cup \Lambda_+^{\text{adm}}} [J]$

**repeat**

  Compute the admissible set  $\Lambda_+^{\text{adm}}$ , as in (56).  
  Compute the hierarchical surpluses  $s_{\ell}$ ,  
   $\forall \ell \in \Lambda_+^{\text{adm}}$ , as in (53).  
  Find the multi-index  $\ell \in \Lambda_+^{\text{adm}}$  with the  
  maximum error indicator  $|s_{\ell}|$ .  
  Compute the approximation  $\mathcal{I}_{\Lambda \cup \ell}$ , as in (52).  
  Set  $\Lambda = \Lambda \cup \ell$ .

**until** simulation budget  $B$  is reached;

**Algorithm 1:** Dimension-adaptive interpolation.

where

$$\hat{h}_{\ell_n}(y_n) := \begin{cases} \prod_{k=0}^{\ell_n-1} \frac{g_n^{-1}(y_n) - y_n^{(k)}}{y_n^{(\ell_n)} - y_n^{(k)}}, & \ell_n \neq 0, \\ 1, & \ell_n = 0. \end{cases} \quad (55)$$

Again, by choosing  $g_n$  as the identity map we recover standard hierarchical Lagrange polynomials.

The use of (mapped) hierarchical polynomials has the advantage that the basis functions do not change as new nodes are added. Moreover, the hierarchical surpluses  $s_{\ell}$  can be interpreted as error indicators, quantifying the contribution of the interpolation node  $\hat{\mathbf{y}}^{(\ell)}$  to the already available approximation. This interpretation motivates the adaptive construction of the sparse grid approximation based on a posteriori error estimates. We consider a dimension-adaptive scheme, similar to the ones employed in [28, 29, 70, 30, 55], with minor modifications to address the case of complex QoIs. The scheme is presented in Algorithm 1. A detailed description follows.

Given a downward-closed multi-index set  $\Lambda$ , as well as the corresponding approximation  $\mathcal{I}_{\Lambda} [J]$  and grid  $Z_{\Lambda}$ , we define the set of admissible neighbors  $\Lambda_+^{\text{adm}}$ , such that

$$\Lambda_+^{\text{adm}} := \{\ell \in \Lambda_+ : \ell \notin \Lambda \text{ and } \{\ell\}_- \subset \Lambda\}. \quad (56)$$

Expanding  $\Lambda$  with admissible multi-indices  $\ell \in \Lambda_+^{\text{adm}}$  guarantees that (50) is satisfied, and we thus construct a sequence of nested downward-closed sets [28]. In this work, the error indicator corresponding to each multi-index  $\ell \in \Lambda_+^{\text{adm}}$  is chosen to be the modulus  $|s_{\ell}|$  of the corresponding complex hierarchical surplus, however, other choices are possible, e.g.  $\max(|\text{Re}\{s_{\ell}\}|, |\text{Im}\{s_{\ell}\}|)$ . We update  $\Lambda$  with the multi-index  $\ell \in \Lambda_+^{\text{adm}}$  corresponding to the maximum error indicator  $|s_{\ell}|$ . The grid of interpolation nodes  $Z_{\Lambda}$  and the approximation  $\mathcal{I}_{\Lambda}$  are updated accordingly. This procedure is continued iteratively, until a budget of model evaluations  $B$  is reached. This criterion can be formulated as

$$\#Z_{\Lambda \cup \Lambda_+^{\text{adm}}} \geq B, \quad (57)$$

where  $\#$  denotes the cardinality of a set. If an approximation is not readily available, the algorithm is initiated with

$\Lambda = \{(0, 0, \dots, 0)\}$ . After the termination of the algorithm, the approximation is constructed using the set  $\Lambda \cup \Lambda_+^{\text{adm}}$ .

### 3.3. Adjoint error estimation and adaptivity

We aim to improve Algorithm 1 by using of an adjoint error indicator to steer adaptivity. Adjoint error estimation is well established in the context of the FEM, see [77] and the references therein. It has been considered in a stochastic/parametric context [52, 53, 78], as well as for Clenshaw-Curtis adaptivity [54, 55]. Due to the exponential growth of Clenshaw-Curtis nodes, adjoint error estimation can result in a significant reduction of computational cost. In this work, we demonstrate that adjoint techniques can be beneficial for Leja adaptivity, too.

In this section we assume that  $J(\mathbf{y}) = J_{\mathbf{y}}(\mathbf{u}(\mathbf{y}))$ ,  $J_{\mathbf{y}} : V \rightarrow \mathbb{C}$ , is a linear functional with respect to  $\mathbf{u}(\mathbf{y})$ . Generalizations to non-linear functionals are also possible, as in [79, Chapter 3.2]. We rewrite the primal problem (17) as an operator equation:  $\forall \mathbf{y} \in \Xi$ , find  $\mathbf{u}(\mathbf{y}) \in V$ , such that

$$\langle L_{\mathbf{y}} \mathbf{u}(\mathbf{y}), \mathbf{v} \rangle = a_{\mathbf{y}}(\mathbf{u}(\mathbf{y}), \mathbf{v}) = l_{\mathbf{y}}(\mathbf{v}) \quad \forall \mathbf{v} \in V, \quad (58)$$

where  $L_{\mathbf{y}} : V \rightarrow V^*$  denotes the primal operator and  $V^*$  the dual space to  $V$ . The dual problem is given as:  $\forall \mathbf{y} \in \Xi$ , find  $\mathbf{z}(\mathbf{y}) \in V$ , such that

$$\langle \mathbf{w}, L_{\mathbf{y}}^* \mathbf{z}(\mathbf{y}) \rangle = a_{\mathbf{y}}(\mathbf{w}, \mathbf{z}(\mathbf{y})) = J_{\mathbf{y}}(\mathbf{w}) \quad \forall \mathbf{w} \in V, \quad (59)$$

where  $L_{\mathbf{y}}^* : V \rightarrow V^*$  denotes the adjoint operator defined by

$$\langle L_{\mathbf{y}} \mathbf{u}, \mathbf{v} \rangle = \langle \mathbf{u}, L_{\mathbf{y}}^* \mathbf{v} \rangle \quad \forall \mathbf{u}, \mathbf{v} \in V, \quad \forall \mathbf{y} \in \Xi. \quad (60)$$

The so-called primal-dual equivalence

$$J_{\mathbf{y}}(\mathbf{u}(\mathbf{y})) = \langle \mathbf{u}(\mathbf{y}), L_{\mathbf{y}}^* \mathbf{z}(\mathbf{y}) \rangle = \langle L_{\mathbf{y}} \mathbf{u}(\mathbf{y}), \mathbf{z}(\mathbf{y}) \rangle = l_{\mathbf{y}}(\mathbf{z}(\mathbf{y})) \quad (61)$$

follows directly from these definitions. Given (mapped) polynomial approximations  $\tilde{\mathbf{u}}, \tilde{\mathbf{z}}$  of the mappings  $\mathbf{u}, \mathbf{z} : \Xi \rightarrow V$ , we are interested in the error

$$\eta(\mathbf{y}) = J_{\mathbf{y}}(\mathbf{u}(\mathbf{y}) - \tilde{\mathbf{u}}(\mathbf{y})) \quad (62)$$

$$= a_{\mathbf{y}}(\mathbf{u}(\mathbf{y}) - \tilde{\mathbf{u}}(\mathbf{y}), \mathbf{z}(\mathbf{y})) \quad (63)$$

$$= l_{\mathbf{y}}(\mathbf{z}(\mathbf{y})) - a_{\mathbf{y}}(\tilde{\mathbf{u}}(\mathbf{y}), \mathbf{z}(\mathbf{y})). \quad (64)$$

Even if  $\tilde{\mathbf{u}}, \tilde{\mathbf{z}}$  are replaced by their finite element counterparts, the error according to (64) is not readily computable, as it would require the computation of the adjoint  $\mathbf{z}$  for all  $\mathbf{y} \in \Xi$ . Following [52, 53], we propose to use the error indicator

$$\tilde{\eta}(\mathbf{y}) = a_{\mathbf{y}}(\mathbf{u}(\mathbf{y}) - \tilde{\mathbf{u}}(\mathbf{y}), \tilde{\mathbf{z}}(\mathbf{y})) \quad (65)$$

$$= l_{\mathbf{y}}(\tilde{\mathbf{z}}(\mathbf{y})) - a_{\mathbf{y}}(\tilde{\mathbf{u}}(\mathbf{y}), \tilde{\mathbf{z}}(\mathbf{y})). \quad (66)$$

By exploiting the continuity of the sesquilinearform  $a_{\mathbf{y}}(\cdot, \cdot)$ , it can be shown that the error indicator (66) converges faster than the mapped polynomial approximations  $\tilde{\mathbf{u}}, \tilde{\mathbf{z}}$

$$|\eta(\mathbf{y}) - \tilde{\eta}(\mathbf{y})| = |a_{\mathbf{y}}(\mathbf{u}(\mathbf{y}) - \tilde{\mathbf{u}}(\mathbf{y}), \mathbf{z}(\mathbf{y}) - \tilde{\mathbf{z}}(\mathbf{y}))| \quad (67)$$

$$\leq C \|\mathbf{u}(\mathbf{y}) - \tilde{\mathbf{u}}(\mathbf{y})\|_V \|\mathbf{z}(\mathbf{y}) - \tilde{\mathbf{z}}(\mathbf{y})\|_V. \quad (68)$$

In particular, considering for the moment the univariate case  $N = 1$ , for simplicity, and assuming that  $\mathbf{u}, \mathbf{z}$  can be extended analytically onto open Bernstein ellipses  $E_{\hat{r}_u}, E_{\hat{r}_z}$ , respectively and that there exists uniform bounds on their extensions. Then, we obtain

$$\|\eta(\mathbf{y}) - \tilde{\eta}(\mathbf{y})\|_\infty \leq C_1(1 + \Delta_M)^2 \frac{C_2(\hat{r}_u \hat{r}_z)^{-M}}{(1 - \hat{r}_u)(1 - \hat{r}_z)}, \quad (69)$$

for  $M$ -point approximations of both  $\mathbf{u}$  and  $\mathbf{z}$ . Hence, for  $\hat{r}_u = \hat{r}_z$ ,  $\tilde{\eta}$  exhibits twice the rate of geometric convergence.

We proceed by discussing the necessary adaptations to Algorithm 1, in order to incorporate the adjoint error indicator (66). Additionally to the (mapped) polynomial approximation (52) of the single-valued and complex QoI, one needs to create (mapped) polynomial approximations  $\tilde{\mathbf{u}}(\mathbf{y}), \tilde{\mathbf{z}}(\mathbf{y})$  of the vector-valued primal and dual solution. Those can be obtained by using vector coefficients  $\mathbf{u}_\ell, \mathbf{z}_\ell \in \mathbb{C}^{N_{\text{DoF}}}$  instead of the single-valued coefficients  $s_\ell \in \mathbb{C}$  in (52). The approximations are constructed with the same multi-index set  $\Lambda$  as for the QoI, using the same mapped polynomials  $\hat{H}_\ell(\mathbf{y})$ .

Following [54], we carry out the algorithmic modifications in the dimension-adaptive scheme. While Algorithm 1 uses the error indicators  $|s_\ell|, \forall \ell \in \Lambda_+^{\text{adm}}$ , by solving the respective linear system, we suggest the use of the adjoint-based error indicators  $|\tilde{s}_\ell|$ , where  $\tilde{s}_\ell = \tilde{\eta}(\hat{\mathbf{y}}^{(\ell)})$ . As before, we choose the multi-index with the maximum error indicator, solve the corresponding linear system and update the approximations of the primal and the dual solution, as well as of the QoI. This scheme is summarized in Algorithm 2. After the termination of the algorithm, the approximation can be constructed with the set  $\Lambda \cup \Lambda_+^{\text{adm}}$ , such that the already computed adjoint-based error indicators are used as the hierarchical surpluses corresponding to the admissible neighbors, i.e.  $s_\ell = \tilde{s}_\ell, \forall \ell \in \Lambda_+^{\text{adm}}$ . The error indicator (66) can be further employed in order to improve the (mapped) polynomial surrogate model of the QoI. In particular, one can replace the single-valued QoI  $J(\mathbf{y})$  by

$$\tilde{J}(\mathbf{y}) = \mathcal{I}_\Lambda[J](\mathbf{y}) + \tilde{\eta}(\mathbf{y}), \quad (70)$$

such that the computed mapped polynomial approximation is corrected by the adjoint-error indicator, before continuing with further approximation refinements using Algorithm 1. We emphasize that no additional linear equation system has to be solved in order to evaluate (70).

**Remark 3.1.** Relating the methodology of this section to the scattering in periodic media, the linear functional is given by

$$S_{\alpha,mn}(\mathbf{y}) = \underbrace{(\mathbf{E}_T(\mathbf{y}), \pi_T [\mathbf{E}_{\alpha,mn}])}_{=J(\mathbf{E})} - (\mathbf{E}_T^{\text{inc}}, \pi_T [\mathbf{E}_{\alpha,mn}])_{\Gamma_{z^+}},$$

where  $\alpha \in \{\text{TE}, \text{TM}\}$ .

The strong formulation of the adjoint problem (59) reads

$$\nabla \times \left( \frac{1}{\mu_r^*} \nabla \times \mathbf{z} \right) - \omega^2 \mu_0 \epsilon^* \mathbf{z} = 0 \quad \text{in } D, \quad (71a)$$

**Data:**  $\mathbf{A}_{\text{dof}}(\mathbf{y}), \mathbf{f}_{\text{dof}}(\mathbf{y}), \mathbf{J}_{\text{dof}}(\mathbf{y}), \mathbf{g}, \Lambda, B$

**Result:** sparse grid  $Z_{\Lambda \cup \Lambda_+^{\text{adm}}}$ ,  
approximation  $\mathcal{I}_{\Lambda \cup \Lambda_+^{\text{adm}}} [J]$

**repeat**

Compute the admissible set  $\Lambda_+^{\text{adm}}$ , as in (56).

Compute the error indicators  $|\tilde{s}_\ell|$ , where

$$\tilde{s}_\ell = \tilde{\eta}(\hat{\mathbf{y}}^{(\ell)}), \forall \ell \in \Lambda_+^{\text{adm}}.$$

Find the multi-index  $\ell \in \Lambda_+^{\text{adm}}$  with the maximum error indicator.

Compute the hierarchical surpluses  $s_\ell, \mathbf{u}_\ell, \mathbf{z}_\ell$  as in (53), by solving the linear systems for primal and dual solution.

Compute the approximation  $\mathcal{I}_{\Lambda \cup \ell}$ , as in (52), and the corresponding approximations of primal and dual solution.

$$\text{Set } \Lambda = \Lambda \cup \ell.$$

**until** stopping criterion fulfilled;

**Algorithm 2:** Adjoint error-based, dimension-adaptive interpolation.

$$\mathbf{z}_T|_{\Gamma_{x^+}} e^{-j\psi_x} = \mathbf{z}_T|_{\Gamma_{x^-}} \quad \text{on } \Gamma_{x^+} \cup \Gamma_{x^-}, \quad (71b)$$

$$\mathbf{z}_T|_{\Gamma_{y^+}} e^{-j\psi_y} = \mathbf{z}_T|_{\Gamma_{y^-}} \quad \text{on } \Gamma_{y^+} \cup \Gamma_{y^-}, \quad (71c)$$

$$\mathbf{z}_t = 0 \quad \text{on } \Gamma_{z^-}, \quad (71d)$$

$$\mathbf{e}_z \times \left( \frac{j}{\omega \mu_0} \nabla \times \mathbf{z} \right) + \bar{\mathcal{G}} = \bar{\mathcal{F}} \quad \text{on } \Gamma_{z^+}, \quad (71e)$$

where  $\bar{\mathcal{G}}$  and  $\bar{\mathcal{F}}$  are defined in Appendix A.

Discretization of the adjoint problem (59) yields the discrete matrix equation

$$\mathbf{A}_{\text{dof}}^H \mathbf{z}_{\text{dof}} = \mathbf{P}^H \mathbf{J} = \mathbf{J}_{\text{dof}}, \quad \text{where } \mathbf{J} \in \mathbb{C}^{N_h} \quad (72)$$

and the discrete version of the error indicator (66) reads

$$\tilde{\eta}_h(\mathbf{y}) = \tilde{\mathbf{z}}_{\text{dof}}^H(\mathbf{y}) \mathbf{f}_{\text{dof}}(\mathbf{y}) - \tilde{\mathbf{z}}_{\text{dof}}^H(\mathbf{y}) \mathbf{A}_{\text{dof}}(\mathbf{y}) \tilde{\mathbf{c}}_{\text{dof}}(\mathbf{y}). \quad (73)$$

Note that the dual solution can be obtained with negligible cost in many cases, e.g. if the primal problem is solved with a sparse LU decomposition  $\mathbf{A}_{\text{dof}} = \mathbf{L}\mathbf{U}$ , for the respective dual problem we obtain

$$\mathbf{A}_{\text{dof}}^H = (\mathbf{L}\mathbf{U})^H = \mathbf{U}^H \mathbf{L}^H. \quad (74)$$

## 4. Application

We apply the UQ methods presented in Section 3 to an optical grating coupler model [5, 80]. First, we describe the parametrized numerical model. Then, we quantify the impact of geometric and material uncertainties for the case of single-frequency excitation. We consider both the dimension-adaptive collocation method with (mapped) Leja nodes and a (mapped) gPC approximation, where discrete projection is used to determine the coefficients. gPC is used here mainly for comparison. Additionally, the decay of the gPC coefficients gives insight into the regularity of the input-to-output mapping, justifying the use of spectral methods numerically.

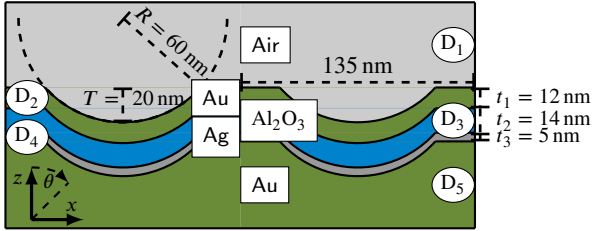


Figure 10: Design of considered optical grating coupler.

Finally, we consider the case of a variable frequency and discuss the necessary adaptations for performing UQ for resonances. Both the deterministic numerical model and the UQ studies rely on open-source software.

For general periodic structures, we must distinguish between two types of uncertainties. In this work we focus on *global* uncertainties, i.e. we assume that all unit cells are identically affected, modeling a systematic offset in the fabrication process. We do not address *local* uncertainties leading to a violation of the periodicity and different unit cells. Readers interested in the latter case are referred to [59] for a relevant study.

#### 4.1. Numerical model

The considered grating coupler [5] couples power from an incident transverse magnetic (TM) polarized plane wave, such that

$$\pi_T [E^{inc}] = \pi_T [E_{TM,00}], \quad \text{at } \Gamma_{z^+},$$

with propagation direction  $\theta^{inc} = 53^\circ$ ,  $\phi^{inc} = 0^\circ$ , directly into a MIM plasmon mode.

The structure's design, shown in Fig. 10, is assumed to be periodic in the  $x$  direction and infinitely extended in the  $y$  direction. The reflection coefficients (12) at the upper boundary  $\Gamma_{z^+}$  correspond to the coupling efficiency of the structure, such that larger reflection coefficients indicate a lower coupling efficiency. Therefore, the scattering parameter  $S := S_{TM,00}$  is considered as the QoI in the following. Note that we focus on the fundamental reflection coefficient  $S_{TM,00}$  because, for this particular model, all other scattering parameters have negligible amplitudes.

We model the material properties based on measurement data for noble metals provided by Johnson and Christy in [81] and presented in Table 1. We focus on the frequency range  $f_{min} = 400$  THz to  $f_{max} = 430$  THz, see Fig. 11. The data is experimentally determined by reflectivity studies and is therefore given in terms of the refractive indices  $n$  and the extinction coefficients  $\kappa$  for gold and silver, respectively. From those, one obtains the complex permittivity as in [2, Chapter 1.1], i.e.

$$\epsilon = (n^2 - \kappa^2 - j(2n\kappa)) \epsilon_0. \quad (75)$$

The data is provided for discrete frequency sample points. Therefore, we need to interpolate in between those sample

points in order to obtain the dispersive behaviour of the permittivity  $\epsilon(\omega)$ . Since we only focus on a rather small frequency range, we apply polynomial interpolation

$$n^{Au}(\omega) = \sum_{i=0}^2 n_i^{Au} l_i(\omega), \quad (76)$$

$$n^{Ag}(\omega) = \sum_{i=0}^2 n_i^{Ag} l_i(\omega), \quad (77)$$

$$\kappa^{Au}(\omega) = \sum_{i=0}^2 \kappa_i^{Au} l_i(\omega), \quad (78)$$

$$\kappa^{Ag}(\omega) = \sum_{i=0}^2 \kappa_i^{Ag} l_i(\omega), \quad (79)$$

where

$$l_i(\omega) = \prod_{j=0, j \neq i}^2 \frac{\omega - \omega_j}{\omega_i - \omega_j}, \quad \omega_i = 2\pi f_i,$$

are 2nd order Lagrange polynomials and  $f_i, n_i^{Au}, \kappa_i^{Au}, n_i^{Ag}, \kappa_i^{Ag}, i = 0, 1, 2$  are given.

We proceed with the implementation of the deterministic numerical model, as well as its parametrization. The periodic mesh for the nominal design, needed for imposing the quasi-periodic boundary conditions (5a), (5b), is created using GMSH [82]. Since for this particular structure only the fundamental Floquet modes propagate and all higher order modes are attenuated to a negligible amplitude at  $\Gamma_{z^+}$ , we can use the first order Floquet boundary condition (113). We use FENiCS [83] as FE library to assemble the FE matrix  $\mathbf{A}$  and right-hand side (RHS)  $\mathbf{f}$  (see (119)), as well as the linear functional  $\mathbf{J}_{dof}$  used for the numerical approximation of the scattering parameter

$$S_{TM,00} = (\mathbf{E}_T - \mathbf{E}_T^{inc}, \pi_T [E_{TM,00}])_{\Gamma_{z^+}} \approx \mathbf{J}_{dof}^T \mathbf{c}_{dof} - 1.$$

Since FENiCS 2017.2.0 is not able to deal with complex numbers, we assemble the real and the imaginary parts of the matrix and the vectors separately. We then use NUMPY and SCIPY to impose the quasi-periodic boundary conditions (5a), (5b) and solve the resulting linear system (119) by a sparse LU decomposition, respectively. Using 2nd order Nédélec elements of the 1st kind, we end up with 56 200 degrees of freedom (DoFs) and achieve an accuracy of  $\approx 10^{-3}$  in the scattering parameter. The reference solutions for different frequency sample points are computed with a commercial software [84] employing an adaptively refined mesh of higher order curved elements. Since a sparse LU decomposition is used to solve the resulting linear system, the adjoint solution  $\mathbf{z}_{dof}$  is obtained with negligible costs.

To incorporate changes in the geometry parameters without the need to re-mesh, a design element approach is applied [85]: First, an initial mesh is created using GMSH for the initial geometry parameters  $\mathbf{y}^{nominal}$ . We describe all (material) interfaces, illustrated in Fig. 12 in red color, using non-uniform rational B-splines (NURBS) [86]. Each NURBS

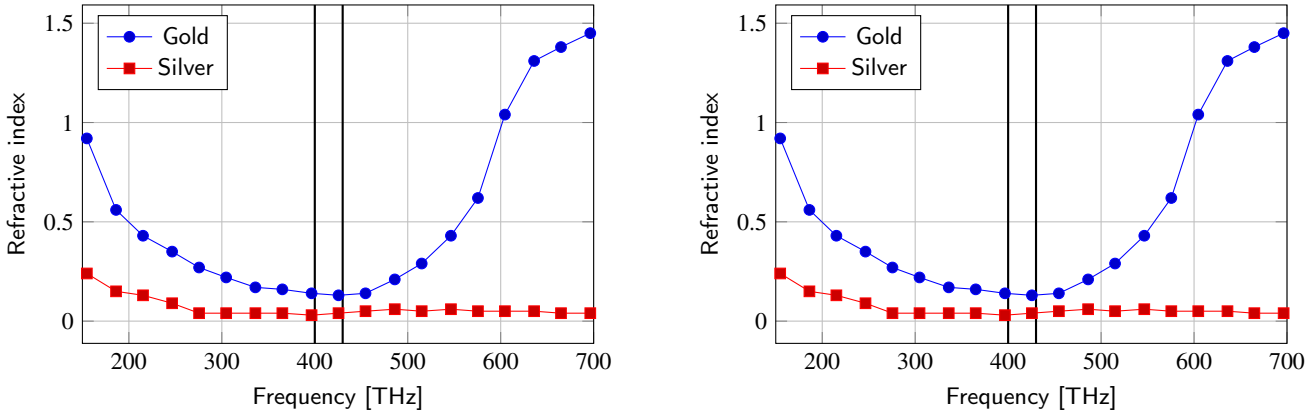


Figure 11: Dispersive optical constants of gold and silver [81]. The black vertical lines define the considered frequency range.

**Table 1**  
Material data, taken from [81].

Index $i$	Energy [eV]	Frequency $f_i$ [THz]	Refractive index $n_i^{\text{Au}}$	Extinction coefficient $\kappa_i^{\text{Au}}$	Refractive index $n_i^{\text{Ag}}$	Extinction coefficient $\kappa_i^{\text{Ag}}$
0	1.64	396.55	$0.14 \pm 0.02$	$4.542 \pm 0.015$	$0.03 \pm 0.02$	$5.242 \pm 0.015$
1	1.76	425.57	$0.13 \pm 0.02$	$4.103 \pm 0.010$	$0.04 \pm 0.02$	$4.838 \pm 0.010$
2	1.88	454.58	$0.14 \pm 0.02$	$3.697 \pm 0.007$	$0.05 \pm 0.02$	$4.483 \pm 0.007$

curve

$$\mathbf{C}_i(\xi; \mathbf{y}) = \sum_{j=0}^n R_j(\xi) \mathbf{P}_{j,i}(\mathbf{y}), \quad \xi \in [0, 1] \quad (80)$$

is a superposition of rational basis functions  $R_j(\xi)$  weighted by control points  $\mathbf{P}_j$ . We then define mappings

$$\mathbf{T}_m(\xi, \eta; \mathbf{y}) = \eta \mathbf{C}_{m,u}(\xi; \mathbf{y}) + (1 - \eta) \mathbf{C}_{m,l}(\xi; \mathbf{y}), \quad m = 1, \dots, M, \quad (81)$$

from the unit square  $[0 \leq \xi \leq 1] \times [0 \leq \eta \leq 1]$  to each design element  $D_i(\mathbf{y})$  (see Fig. 12). Thereby, the subscripts  $u$  and  $l$  refer to the upper and lower NURBS curve of the design element, respectively. Given the initial mesh, for each mesh node  $j$  with coordinates  $\mathbf{x}_j$  inside the design element  $D_m$ , the respective coordinates  $\xi_j, \eta_j$  on the unit square are found

by solving the non-linear root finding problem: find  $\xi_j, \eta_j \in [0, 1]$ , s.t.

$$\mathbf{T}_m(\xi_j, \eta_j; \mathbf{y}^{\text{nominal}}) - \mathbf{x}_j = \mathbf{0}, \quad \mathbf{x}_j \in D_m(\mathbf{y}^{\text{nominal}}). \quad (82)$$

Problem (82) can be reformulated as an optimization problem and is solved here using sequential quadratic programming (SQP) [87, Chapter 18]. In order to ensure convergence of SQP, one might need to choose adequate initial values, which depend on the chosen parametrization of the NURBS curves. Given the coordinates  $\xi_j, \eta_j$  for each mesh node  $j$ , we can deform the mesh by moving the mesh nodes to the new coordinates obtained by evaluating the mapping (81) for different geometry parameters  $\mathbf{y}$ .

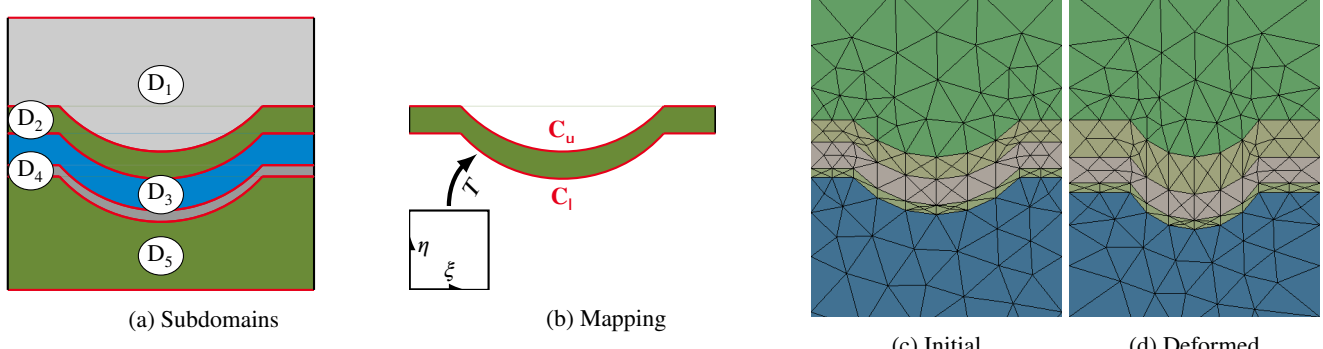


Figure 12: a) design elements. b) mapping from unit square. c) initial mesh (coarse for illustration) for nominal design  $\mathbf{y}^{\text{nominal}}$ . d) deformed mesh for  $R = 40 \text{ nm}$ ,  $t_1 = 20 \text{ nm}$ .

**Table 2**

Uncertain geometrical parameters.

Parameter	Nominal value	Variation
Grating radius $R$	60 nm	$\pm 1.5$ nm
Gold layer thickness $t_1$	12 nm	$\pm 1.5$ nm
Alumina layer thickness $t_2$	14 nm	$\pm 1.5$ nm
Silver layer thickness $t_3$	5 nm	$\pm 1.5$ nm
Grating depth $T$	20 nm	$\pm 1.5$ nm

## 4.2. Single frequency calculations

In this subsection, we consider a fixed frequency  $\omega = 2\pi(414 \text{ THz})$  and  $N = 17$  random input parameters  $\mathbf{Y}$ , in particular the 5 geometrical parameters presented in Table 2 and the 12 material parameters given in Table 1. As introduced in Section 2, both the uncertain geometry and the uncertain material coefficients are modeled by an uncertain complex permittivity  $\epsilon(\mathbf{x}, \mathbf{y})$ , see (13).

We assume that the RVs  $Y_n$ ,  $n = 1, 2, \dots, N = 17$ , are independent, uncorrelated and distributed in the ranges defined by their nominal values and variations. The variations of the material parameters are chosen according to the error estimate provided by Johnson and Christy *based on the instrumental accuracy of the reflection and transmission measurements* [81]. Since no further information on the distributions of those measurement uncertainties are specified, the given error estimate is assumed to correspond to a  $2\sigma$  interval. For the geometrical parameters only small variations in the range of  $\pm 1.5$  nm are considered (with a  $2\sigma$  interval of  $\pm 1$  nm).

Assuming uniformly distributed RVs would keep the parameter realizations bounded in the desired ranges, however, this would be a very restrictive assumption. Normal RVs would be a more realistic choice, which could, however, lead to unphysical parameter realizations, e.g. negative geometry values, due to their unbounded support. In this work, we opt for beta distributions, which have bounded support and can approximate normal distributions for suitable choices of their shape parameters [63, Appendix B]. The shape parameters are chosen based on the results of a series of Kolmogorov-Smirnov fitting tests [88]. Fig. 13 presents such an approximation for the grating depth parameter. The corresponding PDF for each RV  $\{Y_n\}_{n=1}^N$  reads

$$\rho(y_n, l_n, u_n) = \begin{cases} \frac{140(y_n - l_n)^3(u_n - y_n)^3}{(u_n - l_n)^7} & l_n < y_n < u_n, \\ 0 & \text{else,} \end{cases} \quad (83)$$

where  $l_n$  and  $u_n$  denote the lower and upper support bound, respectively.

### 4.2.1. Regularity study - decay of Fourier coefficients

We study the decay of polynomial coefficients to numerically investigate the smoothness of the map from the input parameters to the S-parameter, and thus justify the use of polynomial approximations. To that end, we use gPC expansions based on global orthogonal polynomials [63, 26].

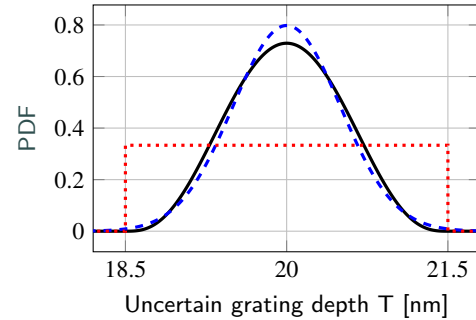


**Figure 13:** Black: PDF of beta distributed grating depth with support in [18.5 nm, 21.5 nm]. Blue, dashed: PDF of normal distribution with  $\mu = 20$  nm and  $\sigma = 0.5$  nm. Red, dotted: PDF of uniform distribution with support in [18.5 nm, 21.5 nm].

We introduce the multi-index  $\mathbf{p} = (p_1, p_2, \dots, p_N) \in \mathbb{N}_0^N$  holding the polynomial degree per parameter and the multivariate polynomials  $\Psi_{\mathbf{p}}(\mathbf{y}) = \prod_{n=1}^N \psi_{p_n}(y_n)$ . The orthogonality condition reads

$$\mathbb{E} [\Psi_{\mathbf{p}} \Psi_{\mathbf{q}}] = \int_{\Xi} \Psi_{\mathbf{p}}(\mathbf{y}) \Psi_{\mathbf{q}}(\mathbf{y}) \rho(\mathbf{y}) d\mathbf{y} = \mathbb{E} [\Psi_{\mathbf{p}}^2] \delta_{\mathbf{p}, \mathbf{q}}, \quad (84)$$

where  $\delta_{\mathbf{p}, \mathbf{q}} = \delta_{p_1, q_1} \delta_{p_2, q_2} \dots \delta_{p_N, q_N}$ . We employ a total-degree polynomial basis  $\{\Psi_{\mathbf{p}} : |\mathbf{p}| = \sum_{n=1}^N p_n \leq p_{\max}\}$ , corresponding to the multi-index set

$$\Lambda_{p_{\max}}^{\text{TD}} := \{\mathbf{p} : |\mathbf{p}| \leq p_{\max}\}. \quad (85)$$

Then, the number of approximation terms is  $M+1 = \frac{(N+p_{\max})!}{N! p_{\max}!}$  and the multivariate gPC approximation reads

$$J(\mathbf{y}) \approx \tilde{J}(\mathbf{y}) = \sum_{|\mathbf{p}| \leq p_{\max}} s_{\mathbf{p}} \Psi_{\mathbf{p}}(\mathbf{y}) = \sum_{\mathbf{p} \in \Lambda_{p_{\max}}^{\text{TD}}} s_{\mathbf{p}} \Psi_{\mathbf{p}}(\mathbf{y}). \quad (86)$$

In the present work, the series coefficients  $s_{\mathbf{p}} \in \mathbb{C}$  are computed by means of pseudo-spectral projection [65, 66], where the series coefficients  $s_{\mathbf{p}}$  are computed as

$$s_{\mathbf{p}} = \frac{\mathbb{E} [J \Psi_{\mathbf{p}}]}{\mathbb{E} [\Psi_{\mathbf{p}}^2]} = \frac{\int_{\Xi} J(\mathbf{y}) \Psi_{\mathbf{p}}(\mathbf{y}) \rho(\mathbf{y}) d\mathbf{y}}{\int_{\Xi} \Psi_{\mathbf{p}}(\mathbf{y}) \Psi_{\mathbf{p}}(\mathbf{y}) \rho(\mathbf{y}) d\mathbf{y}}. \quad (87)$$

In (87), the multivariate integrals of the numerator are typically computed by means of numerical integration [33], e.g. (Quasi-) Monte Carlo (MC) sampling or Gauss quadrature. For Wiener-Askey polynomials [26], the denominator can be determined analytically.

It has been shown, see e.g. [89, Lemma 2] where Legendre polynomials are considered, that the Fourier coefficients  $s_{\mathbf{p}}$  of an  $N$ -variate gPC approximation (86) decay exponentially, provided that the input-output map is analytic. In particular, the estimate

$$|s_{\mathbf{p}}|^2 \leq C e^{-\sum_{n=1}^N g_n p_n}, \quad (88)$$

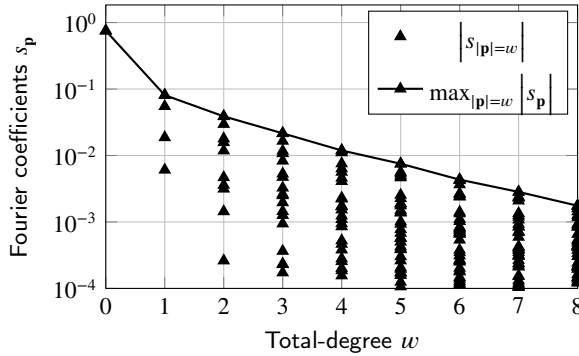


**Figure 14:** Decay of Fourier coefficients of the multivariate gPC approximation for the 4 most sensitive parameters.

has been obtained, where  $C$  and  $g_n$ ,  $n = 1, \dots, N$ , are positive constants independent of  $\mathbf{p}$  and the polynomials are assumed to be normalized, i.e.  $\mathbb{E}[\Psi_{\mathbf{p}} \Psi_{\mathbf{q}}] = \delta_{\mathbf{p}, \mathbf{q}}$ . We consider the maximum of the absolute values of the Fourier coefficients  $s_{\mathbf{p}}$  with fixed total-degree  $w$

$$\begin{aligned} \max_{|\mathbf{p}|=w} |s_{\mathbf{p}}|^2 &\leq \max_{|\mathbf{p}|=w} C e^{-\sum_{n=1}^N g_n p_n} \\ &= C e^{-\min_{|\mathbf{p}|=w} \sum_{n=1}^N g_n p_n} \\ &\leq C e^{-(\min_n g_n)w}. \end{aligned} \quad (89)$$

Based on (89), the maximum Fourier coefficient is expected to decay exponentially with an increasing total-degree  $w$ .

Using the results of the sensitivity analysis presented in Section 4.2.4, we restrict input uncertainties to the 4 most influential parameters, i.e.  $t_1, t_2, T$ , and  $n_1^{\text{Au}}$ , and use CHAOSPY [90] to construct a gPC approximation with a total-degree  $p_{\max} = 8$  polynomial basis. The multivariate integrals of the pseudo-spectral projection (87) are computed by a Gauss quadrature of the same order. All coefficients  $s_{\mathbf{p}}$  are plotted in Fig. 14, where a fast decay, at least sub-exponentially, can indeed be observed. This can be seen as a numerical indicator for smoothness of the approximated mapping  $S(\mathbf{y})$  and, therefore, UQ methods based on spectral (mapped) polynomial approximations, as introduced in Sec. 3, seem to be a good choice for the considered numerical model.

To address the question, for which parameters a conformal map (see Sec. 3.1) should be applied, a second study on the decay of gPC coefficients is performed. This time we consider univariate variations for each of the 17 uncertain parameters given in Tables 1 and 2. For completeness, the frequency is also considered a parameter in this study. On the one hand, we compute the gPC coefficients  $s_{\mathbf{p}}$  as in (87). On the other hand, we employ a conformal map  $\mathbf{g} : \Xi \rightarrow \Xi$  and compute the coefficients

$$\hat{s}_{\mathbf{p}} = \frac{\mathbb{E}[(J \circ \mathbf{g}) \Psi_{\mathbf{p}}]}{\mathbb{E}[\Psi_{\mathbf{p}}^2]}, \quad (90)$$

associated to a gPC approximation of  $J \circ \mathbf{g}$ .

In particular, we use the 9-th order sausage map (28) and plot the coefficient of the respective 8-th order approxima-

tions in Fig. 15. It can be observed that, for the considered setting, the mapping is not beneficial for all material parameters. However, for the slowly converging geometry parameters  $\Delta t_1, \Delta t_2$  a clear improvement can be identified. It should be noted that, since only univariate approximations are needed, the computational cost for such a preliminary study are small compared to a high-dimensional approximation which takes into account interaction effects among parameters.

#### 4.2.2. Adjoint-error indicator

To illustrate the benefits of using the adjoint error indicator presented in Sec. 3.3, we consider here only the thickness of the upper gold layer  $t_1$  and the thickness of the dielectric layer  $t_2$  as input parameters. Fig. 16a shows the S-parameter w.r.t. to small variations of these two sensitive geometry parameters. The previous study showed that, for those two parameters, the use of conformal maps should be computationally beneficial. We construct (mapped) adaptive Leja approximations using Algorithm 1 and the adjoint-based Algorithm 2. The accuracy of the surrogate models is measured using a cross-validation set of  $N^{\text{cv}} = 1000$  parameter realizations  $S^{(i)} := S(\mathbf{y}^{(i)})$ ,  $i = 1, \dots, N^{\text{cv}}$ , drawn according to the underlying PDF, which is used to compute a discrete approximation of the  $L^1_{\rho}$  error

$$\mathbb{E}[|S - \tilde{S}|] \approx \frac{1}{N^{\text{cv}}} \sum_{i=1}^{N^{\text{cv}}} |S^{(i)} - \tilde{S}^{(i)}|. \quad (91)$$

The error (91) is computed for the mapped and adjoint-based approximation, as well as for non-mapped and/or non-adjoint-based variants, for increasing numbers of model evaluations. The corresponding results are shown in Fig. 16b. The plot numerically confirms (68) and shows the doubled convergence order of the adjoint-error indicator. Additionally, it can already be observed that employing the conformal sausage map  $g_S(\cdot; 9)$ , defined in (28), yields to a significant improvement of both convergence orders in the considered setting.

#### 4.2.3. Accuracy and cost of surrogate models

We construct 17 dimensional gPC and (mapped) Leja adaptive approximations, using both Algorithm 1 and the adjoint-based Algorithm 2 for the latter. CHAOSPY is used for the gPC case, while an in-house code was developed for both Leja adaptive algorithms [91]. We compare the resulting surrogate models with respect to accuracy and computational costs.

The computational costs refer to the number of model evaluations needed for the approximation's construction. While straightforward for the gPC and the Leja adaptive Algorithm 1, the estimation of costs is more involved in the case of the adjoint-based Algorithm 2. First, in order to evaluate the duality-based error indicator (73) at a candidate point, it is sufficient to evaluate a residual of (14). Therefore, we distinguish between residual evaluations and solver calls, where in most cases the costs to evaluate the residuals are almost negligible compared to the solver costs, i.e. assembly and sparse

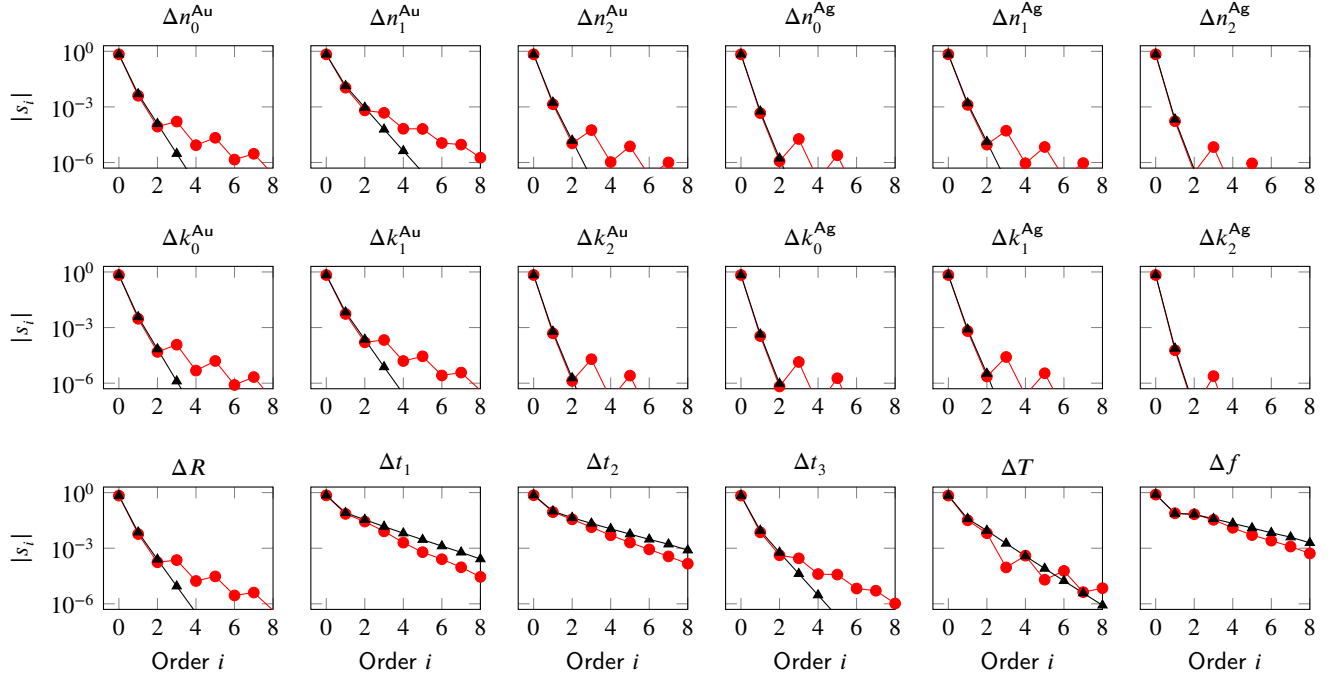


Figure 15: Univariate Fourier coefficient studies using gPC approximations for  $J$  (triangles, black) and  $J \circ g$  (circles, red).

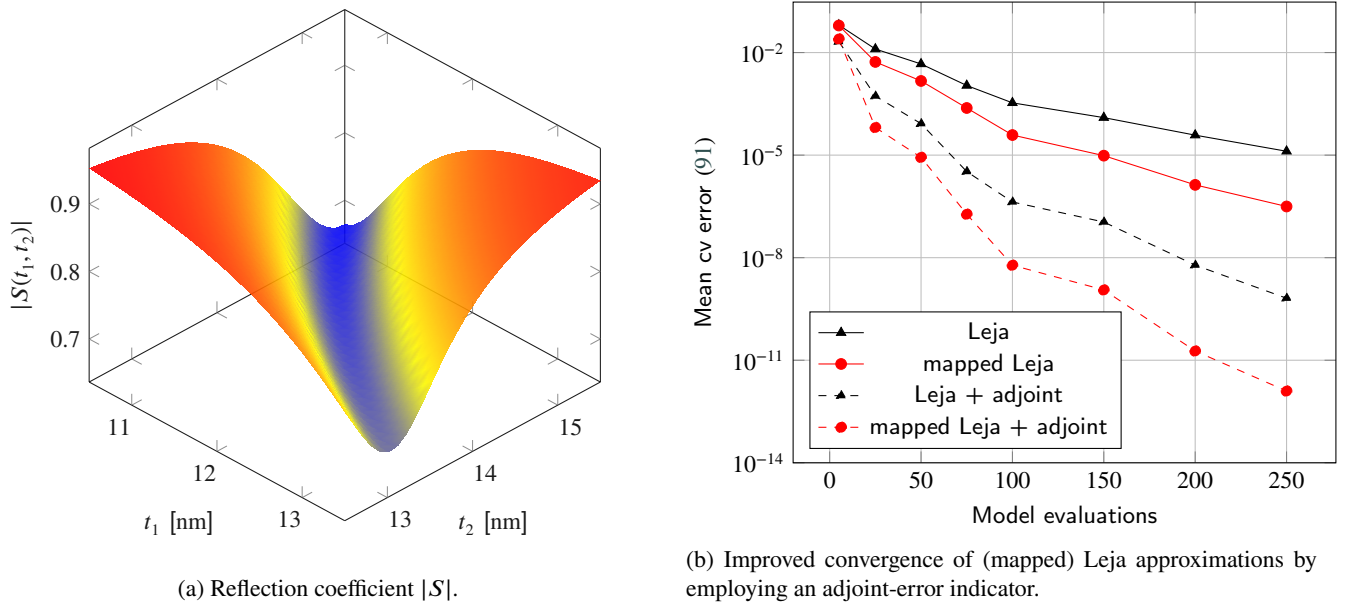


Figure 16: Considering a two dimensional parameter space and a fixed frequency of 414 THz.

LU decomposition of the system matrices  $\mathbf{A}_{\text{dof}}(\mathbf{y})$ . Second, the additional costs for computing the dual solution  $\mathbf{z}$  by forward and backward substitution can also be neglected in most cases, since the primal problem is solved with a sparse LU decomposition.

As before, the accuracy of the surrogate models is measured using a cross-validation set of  $N^{\text{cv}} = 1000$  parameter realizations  $S^{(i)} := S(\mathbf{y}^{(i)})$ ,  $i = 1, \dots, N^{\text{cv}}$ , drawn according to the underlying PDF. In addition to (91), we also con-

sider the maximum error over all sample points

$$\max_{i=1, \dots, N^{\text{cv}}} |S^{(i)} - \tilde{S}^{(i)}|. \quad (92)$$

All accuracy and cost results are presented in Table 3. First, a gPC approximation with a 2nd order total-degree polynomial basis, i.e. 171 Jacobi polynomials, is constructed. The polynomial coefficients are computed with a sparse 2nd order Gauss quadrature formula, resulting in 613 quadrature nodes, accordingly, model evaluations. We set a budget

**Table 3**

Accuracy and computational cost of different polynomial approximations for 17 input RVs. #LU refers to the dominating costs for the assembly and sparse LU decomposition of the system matrices. #FB and #Res denote the number of forward-backward substitutions and residual evaluations, respectively.

	#LU	#FB	#Res	Max. Error (92)	Mean Error (91)
Total-degree gPC (without maps)	<b>613</b>	<b>613</b>	0	$7.61 \times 10^{-1}$	$1.92 \times 10^{-1}$
Ad. Leja (without adjoints/maps)	<b>613</b>	<b>613</b>	0	$8.56 \times 10^{-2}$	$5.53 \times 10^{-3}$
Ad. iso-mapped Leja (without adjoints)	<b>613</b>	<b>613</b>	0	$3.59 \times 10^{-2}$	$4.10 \times 10^{-3}$
Ad. aniso-mapped Leja (without adjoints)	<b>613</b>	<b>613</b>	0	$3.85 \times 10^{-2}$	$4.15 \times 10^{-3}$
Ad. Leja (with adjoints; without maps)	<b>558</b>	1116	<b>613</b>	$8.46 \times 10^{-2}$	$5.49 \times 10^{-3}$
Ad. iso-mapped Leja (with adjoints)	<b>563</b>	1126	<b>613</b>	$3.57 \times 10^{-2}$	$4.09 \times 10^{-3}$
Ad. aniso-mapped Leja (with adjoints)	<b>563</b>	1126	<b>613</b>	$3.82 \times 10^{-2}$	$4.15 \times 10^{-3}$
Ad. aniso-mapped Leja (with adjoints and error correction)	<b>3000</b>	6000	30000	$1.25 \times 10^{-3}$	$1.20 \times 10^{-4}$

$B = 613$  for the classical, i.e. without adjoints or conformal maps, Leja adaptive Algorithm 1, such that its costs are identical to the gPC. As can be seen in Table 3, the Leja adaptive approximation is about one order of magnitude more accurate than the gPC.

Next, we use again Algorithm 1 but employ conformal maps. In particular, we refer with *iso-mapped* to applying the conformal sausage map  $g_S(\cdot; 9)$  for all parameters while *aniso-mapped* refers to the application of the conformal map only to the parameters  $t_1, t_2, T$  (based on the results of the previous subsection). It can be observed that both approaches yield a similar improvement in terms of accuracy, without (relevant) extra computational cost.

For the adjoint-based Algorithm 2, we then compute approximations using again 613 (mapped) polynomials, resulting in errors almost identical to the non-adjoint case. However, since the costs can be predominantly attributed to the  $\approx 560$  solver calls, the costs are reduced. Note that greater (relative) gains can be observed in different settings, e.g. when a smaller computational budget is used or less parameter anisotropy is present in the considered model. In particular, as a numerical test case, we increased material uncertainties by one third and reduced geometric variations to the range of  $\pm 0.25$  nm. In that case the respective computational cost was reduced by more than 50%.

We also note that, in this case, when either no conformal map or the *aniso-mapped* approach is used, both corresponding Leja adaptive approximations, i.e. with and without adjoint error indicators, employ the same multi-index set  $\Lambda$ , albeit slightly permuted. It is also worth noting that the respective surrogate models are not necessarily completely identical, since, on the one hand, the different ordering may lead to slightly different hierarchical surpluses  $s_\ell$  and, on the other hand, after termination Algorithm 1 uses the exact hierarchical surpluses  $s_\ell$  for all  $\ell \in \Lambda_+^{\text{adm}}$ , while the adjoint-based Algorithm 2 uses the estimates  $\tilde{s}_\ell$  instead.

The convergence of the mean error (91) w.r.t. function calls (corresponding to the number of LU decompositions)

of the investigated spectral methods is additionally shown in Fig. 17. Isotropic gPC seems to not show proper convergence. However, it should be noted that we were only able to compute approximations up to order 3 due to the larger number of parameters. The authors are convinced that the errors are just by chance increasing w.r.t. to the order since the asymptotic behavior is not yet reached. This is further explained in Appendix C. However, it can be concluded that the gPC reference solution achieves very poor accuracy with the given computational budget. All considered dimension-adaptive schemes greatly outperform the isotropic gPC. In accordance with the results in Table 3, Fig. 17 illustrates that the application of the conformal map yields to improvement compared to the classical Leja algorithm while, in this setting, there is a negligible difference between the *iso-mapped* and the *aniso-mapped* approach. It shall be clarified that, in contrast to Table 3, the dashed lines in Fig. 17 correspond to the error of the respective adjoint-based error indicator (73) and therefore do not correspond to (mapped) polynomial surrogate models but require the evaluation of a residual of (14) at each cross-validation sample point  $\mathbf{y}^{(i)}$ ,  $i = 1, \dots, N^{\text{cv}}$ .

Finally, as shown in the last row of Table 3, we compute a very accurate surrogate model, by using the adjoint-based Algorithm 2 with a computational budget of 3000 LU decomposition. The adjoint-based approximation is then refined by employing (70) until 30000 polynomials are used, further reducing the error by more than one order of magnitude. It shall be highlighted that the adjoint-based approach results in tremendous computational savings compared to the classical Leja Algorithm 1 since 27000 full model evaluations could be avoided in this particular setting.

As often pointed out in the literature, see e.g. [54], it is inefficient to reduce the stochastic error below the discretization error. Therefore, the stochastic approximation is not further refined and the most accurate surrogate model (Table 3, last row) is in the following used to compute statistical measures of the absolute value of the scattering parameter  $|S|$ .

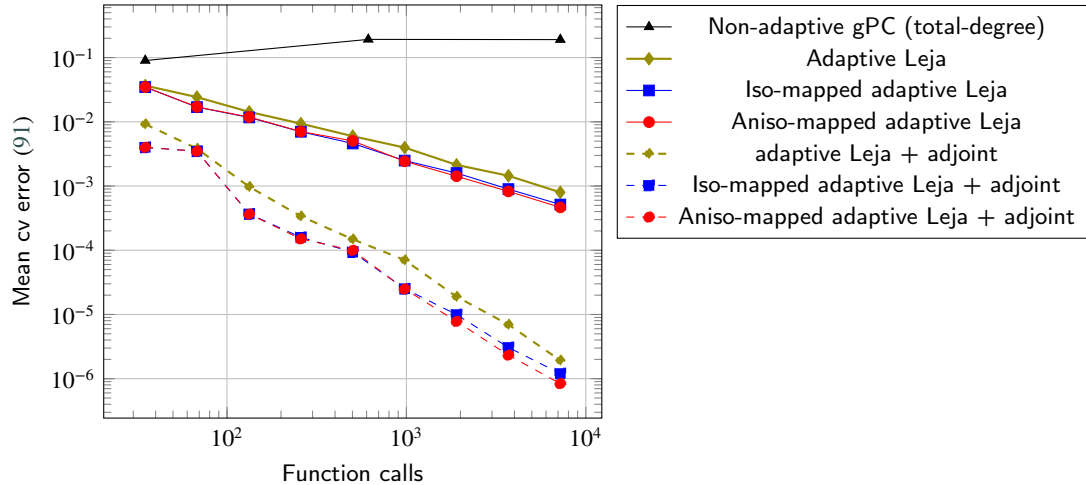


**Figure 17:** Convergence study for the single frequency setting. The adaptive schemes clearly outperform the isotropic approach. Note that the dashed lines correspond to the error of *improved* surrogate models which require the evaluation of FE residuals at each cross-validation point.

#### 4.2.4. Post-processing the surrogate model

Since the (mapped) polynomial surrogate model  $\tilde{S}(\mathbf{y})$  can be evaluated inexpensively, we employ a Monte Carlo-based approach by evaluating the surrogate model on a large number of  $N^{MC}$  parameter sample points, drawn from the joint PDF  $\rho(\mathbf{y})$ . We then use the sample evaluations to estimate statistical moments of  $|S|$ , its PDF, failure probabilities based on specific design criteria, and its sensitivity with respect to the input parameters.

The expected value  $\mathbb{E}[|S|]$  and the variance  $\mathbb{V}[|S|]$  are estimated as

$$\mathbb{E}[|S|] = \int_{\Xi} |S(\mathbf{y})| \rho(\mathbf{y}) d\mathbf{y} \approx \frac{1}{N^{MC}} \sum_{i=1}^{N^{MC}} |\tilde{S}^{(i)}|, \quad (93a)$$

$$\begin{aligned} \mathbb{V}[|S|] &= \int_{\Xi} (|S(\mathbf{y})| - \mathbb{E}[|S|])^2 \rho(\mathbf{y}) d\mathbf{y} \\ &\approx \frac{1}{N^{MC} - 1} \sum_{i=1}^{N^{MC}} (|\tilde{S}^{(i)}| - \mathbb{E}[|\tilde{S}|])^2. \end{aligned} \quad (93b)$$

We estimate the failure probability  $\mathcal{F} = P(|S| \geq 1 - \alpha)$  as

$$\begin{aligned} \mathcal{F} &= P(|S| \geq 1 - \alpha) = \int_{S=1-\alpha}^{S=1} \rho_S dS \\ &= \int_{\Xi} \mathcal{I}_{\mathcal{F}}(S(\mathbf{y})) \rho(\mathbf{y}) d\mathbf{y} \approx \frac{1}{N^{MC}} \sum_{i=1}^{N^{MC}} \mathcal{I}_{\mathcal{F}}(\tilde{S}^{(i)}), \end{aligned} \quad (94)$$

where  $\rho_S$  denotes the PDF of  $|S|$  and  $\mathcal{I}_{\mathcal{F}}$  denotes the indicator function

$$\mathcal{I}_{\mathcal{F}}(S) = \begin{cases} 1, & |S| \in [1 - \alpha, 1], \\ 0, & |S| \in [0, 1 - \alpha]. \end{cases} \quad (95)$$

Monte Carlo sampling in combination with surrogate modeling is used for simplicity here. However, it should be noted that equality in (94) for  $N^{cv} \rightarrow \infty$  cannot be guaranteed in

general, see [92] for counter-examples and possible extensions.

The PDF  $\rho_S$  of  $|S|$  is estimated by employing a kernel density estimator

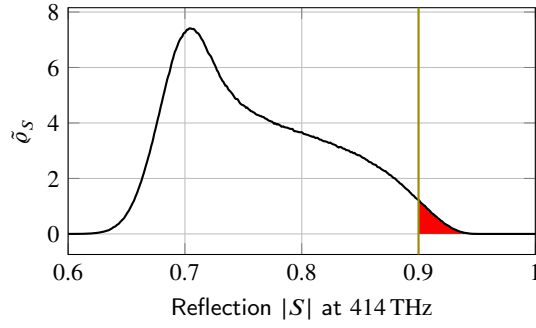
$$\rho_S \approx \tilde{\rho}_T := \frac{1}{hN^{MC}} \sum_{i=1}^{N^{MC}} K\left(\frac{T - |\tilde{S}^{(i)}|}{h}\right) \quad (96)$$

with  $N^{MC} = 10^7$  samples, bandwidth  $h = 10^{-3}$  and the Epanechnikov kernel [93]

$$K(T) := \begin{cases} \frac{3}{4} (1 - T^2), & T \in [-1, 1], \\ 0, & \text{else.} \end{cases} \quad (97)$$

The estimated expected values, standard deviations  $\sqrt{\mathbb{V}}$  and failure probabilities for an increasing sample size  $N^{MC}$  and  $\alpha = 0.1$  are given in Table 18b. The estimated PDF  $\tilde{\rho}_S$  is shown in Fig. 18a.

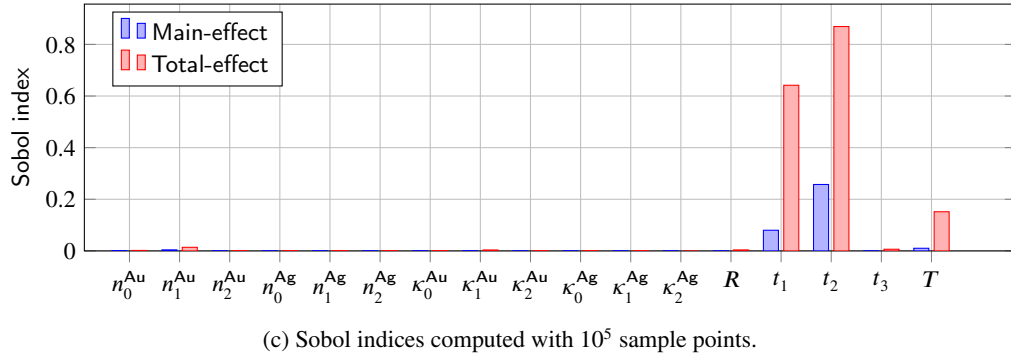
Sensitivity analysis is based on an analysis of variances (ANOVA) [94]. The related metrics are commonly known as Sobol indices, where we will focus on the so-called main-effect (1st order) and total-effect (total order) indices, defined in [95]. In the context of the present work, estimations of the Sobol indices for the magnitude of the scattering parameter shall be based on sampling of the (mapped) polynomial approximation  $\tilde{S} : \Xi \rightarrow \mathbb{C}$ . We use Saltelli's algorithm [96] with  $N^{sens} = 10^5$  sample points, resulting in  $2(17 + 1)10^5 = 3.6 \times 10^6$  surrogate model evaluations. The main-effect and total-effect Sobol indices for each parameter are given in Fig. 18c. The thickness of the dielectric layer  $t_2$ , the thickness of the upper gold layer  $t_1$ , the grating depth  $T$  and the refractive index of the upper gold layer  $n_1^{\text{Au}}$  are identified as the most sensitive parameters. Moreover, since the sum of all main-effect sensitivity indices is approximately 33%, the remaining 67% indicates higher order interactions, and thus strong coupling among the input parameters.



(a) Estimated PDF of scattering parameter. Failure probability illustrated in red color.

$N^{MC}$	$\mathbb{E}$	$\sqrt{\mathbb{V}}$	$\mathcal{F}$
$10^3$	0.7595	0.0661	2.20 %
$10^4$	0.7605	0.0658	1.85 %
$10^5$	0.7606	0.0660	2.04 %
$10^6$	0.7607	0.0660	2.07 %
$10^7$	0.7607	0.0660	2.06 %

(b) Expectation, standard deviation and failure probability, i.e.  $\mathcal{F} = P(|S| \geq 1 - \alpha)$  for  $\alpha = 0.1$ . Surrogate-based Monte Carlo estimation using  $N^{MC}$  sample points.



(c) Sobol indices computed with  $10^5$  sample points.

**Figure 18:** PDF, expectation, standard deviation, failure probability and Sobol indices for 17 beta-distributed input parameters.

It is found that the considered model is highly sensitive to small geometrical variations. In particular, while geometrical variations in a range of only  $\pm 1.5$  nm are considered, their impact is significantly higher than the one attributed to material uncertainty, which was modelled based on the measurement error provided by [81].

### 4.3. Variable Frequency

In Section 4.2, the QoI was considered to be the scattering parameter at a fixed frequency. However, in many applications, one is interested in the uncertainty of the resonance in a given frequency range  $[f_{\min}, f_{\max}]$ , i.e.

$$S_{\text{res}}(\mathbf{y}) = \min_{f \in [f_{\min}, f_{\max}]} |S(f, \mathbf{y})|, \quad (98a)$$

$$f_{\text{res}}(\mathbf{y}) = \arg \min_{f \in [f_{\min}, f_{\max}]} |S(f, \mathbf{y})|. \quad (98b)$$

This poses an additional challenge in performing an efficient UQ. Indeed, the mathematical operations of computing the absolute value and the minimization are not in general differentiable with respect to the uncertain parameters. This is intuitively clear in the presence of more than one resonances inside the parameter range  $[f_{\min}, f_{\max}]$  where the resonance frequency may jump from one resonance to another due to variations in the parameters. Since the convergence properties of polynomial approximations depend crucially on the smoothness of the mapping [25], polynomial approximations of the mappings  $S_{\text{res}} : \Xi \rightarrow [0, 1]$ ,  $f_{\text{res}} : \Xi \rightarrow [f_{\min}, f_{\max}]$  may not converge.

To circumvent this issue, we propose the following workflow: first, we create a polynomial surrogate  $\tilde{S}(f, \mathbf{y})$  of  $S : [f_{\min}, f_{\max}] \times \Xi \rightarrow \mathbb{C}$ , where we exploit that (due to the damping/losses in the considered numerical model) the frequency dependence of the scattering parameter is smooth, as can be observed in Fig. 20. Since the polynomial surrogate can be evaluated inexpensively, we then calculate all statistical measures of the resonance by Monte Carlo estimators which only require square-integrability. In particular, we draw  $N^{MC}$  sample points of the input RVs  $\mathbf{Y}$  and evaluate for each sample point  $\mathbf{y}^{(i)}$  the resonance  $\tilde{S}_{\text{res}}(\mathbf{y})$  and resonance frequency  $\tilde{f}_{\text{res}}(\mathbf{y})$ , by solving the minimization problem for a univariate polynomial

$$\tilde{S}_{\text{res}}^{(i)} := \tilde{S}_{\text{res}}(\mathbf{y}^{(i)}) = \min_{f \in [f_{\min}, f_{\max}]} |\tilde{S}(f, \mathbf{y}^{(i)})|, \quad (99a)$$

$$\tilde{f}_{\text{res}}^{(i)} := \tilde{f}_{\text{res}}(\mathbf{y}^{(i)}) = \arg \min_{f \in [f_{\min}, f_{\max}]} |\tilde{S}(f, \mathbf{y}^{(i)})|. \quad (99b)$$

All statistical measures, e.g. expected values, variances, sensitivity indices, failure probabilities and quantiles, can then be computed from the samples  $\{\tilde{S}_{\text{res}}^{(i)}\}_{i=1}^{N^{MC}}$ ,  $\{\tilde{f}_{\text{res}}^{(i)}\}_{i=1}^{N^{MC}}$ .

We apply the described UQ workflow for the resonance of scattering parameters of the optical grating coupler in a narrow frequency range. In this subsection we exclude geometrical uncertainty such that only the 12 uncertain material parameters given in Table 1 are considered, for which at least a rough estimate of the uncertainty magnitude is available from measurements. We model them as uniformly distributed in the ranges defined by nominal value  $\pm 150\%$  variation. In this way, we can easily compare the results to an

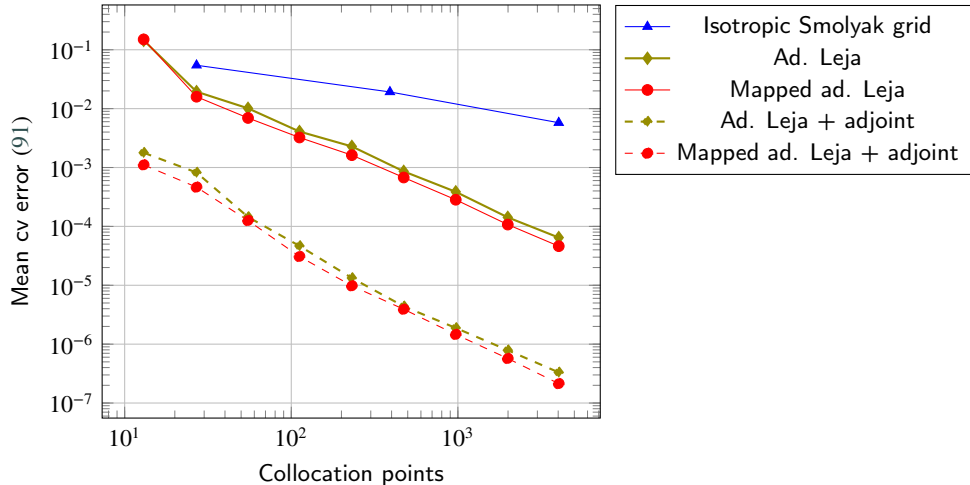


**Figure 19:** Convergence study for variable frequency setting. The adaptive schemes clearly outperform the isotropic approach. Note that the dashed lines correspond to the error of *improved* surrogate models which require the evaluation of FE residuals at each cross-validation point.

**Table 4**

Accuracy and computational cost of different (mapped) polynomial approximations for 13 input RVs. #LU refers to the dominating costs for the assembly and sparse LU decomposition of the system matrices. #FB and #Res denote the number of forward-backward substitutions and residual evaluations, respectively.

	#LU	#FB	#Res	Max. Error (92)	Mean Error (91)
Isotropic Smolyak grid (level 2)	<b>391</b>	391	0	$7.52 \times 10^{-2}$	$1.92 \times 10^{-2}$
Adaptive Leja (without adjoints/maps)	<b>391</b>	391	0	$5.46 \times 10^{-3}$	$1.09 \times 10^{-3}$
Mapped adaptive Leja (without adjoints)	<b>391</b>	391	0	$3.53 \times 10^{-3}$	$8.82 \times 10^{-4}$
Mapped adaptive Leja (with adjoints)	<b>307</b>	614	391	$3.52 \times 10^{-3}$	$8.84 \times 10^{-4}$
Mapped adaptive Leja (with adjoints and error correction)	<b>307</b>	614	2000	$8.31 \times 10^{-4}$	$1.77 \times 10^{-4}$

isotropic Smolyak approach, which is often formulated for uniform random variables. Moreover, considering uniform distributions for the adaptive collocation method is reasonable in general, as accurate tail approximations can be obtained in this way. The true, possibly non-uniform, distribution can still be taken into account afterwards using a suitable random number generator for sampling the surrogate model.

Following the aforementioned workflow, we first create a surrogate model for the scattering parameter  $S : [f_{\min}, f_{\max}] \times \Xi \rightarrow \mathbb{C}$ , where  $\mathbf{y}$  now corresponds to the 12 parameters  $n_i^{\text{Au}}, \kappa_i^{\text{Au}}, n_i^{\text{Ag}}, \kappa_i^{\text{Ag}}, i = 0, 1, 2$ . We apply the adaptive Leja Algorithms 1 and 2 to construct polynomial approximations of the numerical model  $\tilde{S}(f, \mathbf{y})$ . As in the single frequency case, we employ the error metrics (91) and (92) on a cross-validation set of  $N^{\text{cv}} = 10^3$  sample points. Results are given in Table 4 and Fig. 19. We additionally construct isotropic Smolyak sparse-grids [97] using Gauss-Legendre nodes for the 13-dimensional parameter space  $[f_{\min}, f_{\max}] \times \Xi$ . Comparing the isotropic sparse grid approximation to the dimension adaptive one, the latter is found to be clearly superior in terms of accuracy. According to Fig. 15 the conformal sausage

map is beneficial for the frequency parameter but not for the material parameters. Therefore it is only applied for the frequency. However, it still yields a noticeable improvement. Exploiting the adjoint error indicator (73) either increases the accuracy or decreases the computational costs further. Finally, we obtain a very accurate surrogate model using 2000 polynomials and only 307 sparse LU decompositions. Cross-validation indicates that the parametric error is slightly below the FE discretization error.

Using the accurate polynomial model  $\tilde{S}(f, \mathbf{y}^{(i)})$  (Table 4, last row), we perform UQ for the resonance (99b). After drawing  $N^{\text{MC}} = 10^6$  sample points  $\{\mathbf{y}^{(i)}\}_{i=1}^{N^{\text{MC}}}$  from the joint PDF, we obtain  $N^{\text{MC}}$  univariate polynomials  $\tilde{S} : [f_{\min}, f_{\max}] \rightarrow \mathbb{C}$ . For each polynomial, we solve the minimization problem (99b) using SQP [87, Chapter 18]. In order to ensure that the global minimum is found, one can restart the algorithm with different initial values. For this particular model,  $n_{\text{init}} = 3$  different initial values at  $\{400, 415, 430\}$  THz are used.

As an illustration, Fig. 20 shows the frequency response and the resonance frequency for 10 random realizations of the input parameters. Table 5 presents expected values and standard deviations for the resonance frequency  $f_{\text{res}}$ , as well

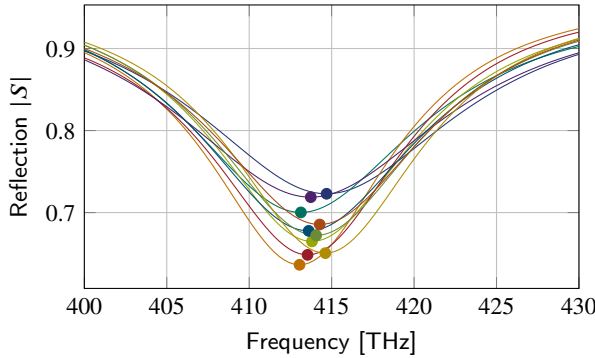


**Figure 20:** Frequency response for 10 random parameter realizations  $\mathbf{y}^{(i)}$ . Dots illustrate resonances.

**Table 5**

UQ for the resonance of the S-parameter in a narrow frequency range: Expectation, standard deviation and failure probability, i.e.  $\mathcal{F}_{\text{res}} = P(|S_{\text{res}}| \geq 0.7)$ .

	$\mathbb{E}$	$\sqrt{\mathbb{V}}$	$\mathcal{F}_{\text{res}}$
$ S_{\text{res}} $	0.683	0.026	32.6%
$f_{\text{res}}$ [THz]	413.822	0.484	–

as the corresponding S-parameter value  $|S_{\text{res}}|$ . Additionally, we estimate the failure probability  $\mathcal{F}_{\text{res}} = P(|S_{\text{res}}| \geq 0.7)$ . All results are computed using Monte Carlo estimators with  $N^{\text{MC}} = 10^5$  sample points of the surrogate model. The results underline that the uncertainty in the input parameters affects the computed resonance.

## 5. Conclusion

In this work we presented an efficient method to quantify uncertainties of the scattering parameter, assuming a moderately large number of input RVs. Dimension adaptivity in combination with an adjoint-error indicator and conformal maps are confirmed to be a promising technique to delay the curse-of-dimensionality, even in presence of poles in the complex plane. For the considered FE model of an optical grating coupler, the comparison of the proposed Leja algorithm with total degree gPC and isotropic Smolyak sparse grids shows significant gains in both accuracy and computational costs. In particular, with the adaptive scheme we were able to consider up to 17 parameters and achieve an accuracy of  $\approx 10^{-3}$ .

In order to perform efficient UQ for the resonance of frequency-dependent scattering parameters, a polynomial surrogate model was created by treating the excitation frequency as an additional parameter. Exploiting that the surrogate model can be inexpensively evaluated, all statistical measures were then calculated by Monte Carlo estimators which only require square integrability. It was further observed that, in the multivariate case, the maximum of the Fourier coefficients with fixed total degree, decays fast, at least sub-exponentially. This indicates smoothness of the output with respect to the input parameters and underlines that polyno-

mial approximations are well-suited for this model, at least for moderate sizes of the parameter variability and frequency range. To consider wider frequency ranges with possible poles in combination with large geometric uncertainties, a combination of polynomial and rational approximations is a topic of future research.

For the considered optical grating coupler, according to Sobol-sensitivity measures, geometrical parameters have been found to be the dominant source of input uncertainty. Although the modeling of their probability distributions could not be based on measurement data yet, this conclusion is substantiated by the very conservative choice of geometrical standard deviations.

## Acknowledgments

The authors would like to thank R. Schuhmann for valuable discussions on the the topic of UQ in plasmonics, in particular for pointing out relevant quantities to compute. N. Georg's work is funded by the DFG grant RO4937/1-1. The work of N. Georg, D. Loukrezis and S. Schöps is also supported by the *Excellence Initiative* of the German Federal and State Governments and the Graduate School of Computational Engineering at Technische Universität Darmstadt.

## A. Floquet boundary condition

To truncate the structure in the non-periodic direction at  $\Gamma_{z^+}$ , a Floquet absorbing boundary condition can be derived by splitting the electric field in the unbounded, homogeneous region  $z \geq z^+$  as

$$\mathbf{E} = \mathbf{E}^{\text{inc}} + \mathbf{E}^{\text{sc}}, \quad (100)$$

where  $\mathbf{E}^{\text{inc}}$  and  $\mathbf{E}^{\text{sc}}$  represent the known incident field and the unknown scattered field, respectively. As derived in [98, Chapter 3] and [99, Chapter 12.2.1], the scattered field  $\mathbf{E}^{\text{sc}}$  can be represented as an infinite series of Floquet modes

$$\mathbf{E}^{\text{sc}} = \sum_{\substack{m,n \in \mathbb{Z} \\ \alpha \in \{\text{TE, TM}\}}} c_{\alpha,mn} \mathbf{E}_{\alpha,mn} e^{-j\kappa_{mn}(z-z^+)}, \quad (101)$$

where

$$\begin{aligned} \mathbf{E}_{\text{TE},mn} &:= \frac{e^{-j(k_{xm}x+k_{yn}y)} (k_{yn}\mathbf{e}_x - k_{xm}\mathbf{e}_y)}{\sqrt{d_x d_y} \sqrt{k_{xm}^2 + k_{yn}^2}}, \\ \mathbf{E}_{\text{TM},mn} &:= \frac{e^{-j(k_{xm}x+k_{yn}y)} (k_{xm}\mathbf{e}_x + k_{yn}\mathbf{e}_y - \frac{k_{xm}^2 + k_{yn}^2}{\kappa_{mn}} \mathbf{e}_z)}{\sqrt{d_x d_y} \sqrt{k_{xm}^2 + k_{yn}^2}}, \end{aligned}$$

with

$$k_{xm} := k_x^{\text{inc}} + \frac{2\pi m}{d_x}, \quad (102)$$

$$k_{yn} := k_y^{\text{inc}} + \frac{2\pi n}{d_y}, \quad (103)$$

$$\kappa_{mn} := \sqrt{k_0^2 - k_{xm}^2 - k_{yn}^2}. \quad (104)$$

Thereby, we distinguish between transverse electric (TE) modes  $\mathbf{E}_{\text{TE},mn}$  and TM modes  $\mathbf{E}_{\text{TM},mn}$ , fulfilling  $\mathbf{E} \perp \mathbf{e}_z$  and  $\mathbf{H} \perp \mathbf{e}_z$ , respectively. There exists only a finite number of propagating modes, i.e.  $\kappa_{mn} \in \mathbb{R}$ , depending on the wavenumber  $k_0$ , the angles of incidence  $\theta^{\text{inc}}$ ,  $\phi^{\text{inc}}$  and the dimensions  $d_x$ ,  $d_y$  of the unit cell.

We introduce the operators  $\pi_t[\mathbf{u}] := \mathbf{e}_z \times \mathbf{u}$  and  $\pi_T[\mathbf{u}] := (\mathbf{e}_z \times \mathbf{u}) \times \mathbf{e}_z$  such that

$$\begin{aligned}\pi_t \left[ \mathbf{H}_{\alpha,mn} e^{-j\kappa_{mn}(z-z^+)} \right] &= \pi_t \left[ \frac{j}{\omega\mu} \nabla \times \left( \mathbf{E}_{\alpha,mn} e^{-j\kappa_{mn}(z-z^+)} \right) \right] \\ &= -Y_{\alpha,mn} \pi_T \left[ \mathbf{E}_{\alpha,mn} e^{-j\kappa_{mn}(z-z^+)} \right],\end{aligned}$$

with

$$Y_{\alpha,mn} := \begin{cases} \frac{\kappa_{mn}}{\omega\mu} & \text{for } \alpha = \text{TE}, \\ \frac{\omega\epsilon}{\kappa_{mn}} & \text{for } \alpha = \text{TM}. \end{cases}$$

The incident plane wave  $\mathbf{E}^{\text{inc}}$  corresponds to the lowest order Floquet modes  $\mathbf{E}_{\alpha,00}$  with modal admittance  $Y^{\text{inc}}$

$$\pi_t[\mathbf{H}^{\text{inc}}] = Y^{\text{inc}} \pi_T[\mathbf{E}^{\text{inc}}], \quad (105)$$

$$Y^{\text{inc}} := \begin{cases} \frac{\sqrt{\epsilon} \cos(\theta^{\text{inc}})}{\sqrt{\mu}} & \text{for } \alpha = \text{TE}, \\ \frac{\sqrt{\epsilon}}{\sqrt{\mu} \cos(\theta^{\text{inc}})} & \text{for } \alpha = \text{TM}. \end{cases} \quad (106)$$

By taking the cross product of the curl of (100) with  $\mathbf{e}_z$ , the magnetic field above the structure is expressed as

$$\begin{aligned}\pi_t[\mathbf{H}] + \sum_{\substack{m,n \in \mathbb{Z} \\ \alpha \in \{\text{TE, TM}\}}} \tilde{c}_{\alpha,mn} Y_{\alpha,mn} \pi_T[\mathbf{E}_{\alpha,mn} e^{-j\kappa_{mn}(z-z^+)}] \\ = 2Y^{\text{inc}} \pi_T[\mathbf{E}^{\text{inc}}].\end{aligned} \quad (107)$$

For any  $\mathbf{u}, \mathbf{v} \in (L^2(\Gamma_{z^+}))^3$ , the space of square-integrable complex vector functions on  $\Gamma_{z^+}$ , we introduce the inner product

$$(\mathbf{u}, \mathbf{v})_{\Gamma_{z^+}} := \int_{\Gamma_{z^+}} \mathbf{u} \cdot \mathbf{v}^* \, d\mathbf{x}, \quad (108)$$

where the superscript  $*$  denotes complex conjugation. Due to the orthogonality of the modal basis, i.e.

$$(\pi_T[\mathbf{E}_{\text{TE},mn}], \pi_T[\mathbf{E}_{\text{TE},ij}])_{\Gamma_{z^+}} = \delta_{mi} \delta_{nj} \quad (109a)$$

$$(\pi_T[\mathbf{E}_{\text{TM},mn}], \pi_T[\mathbf{E}_{\text{TM},ij}])_{\Gamma_{z^+}} = \delta_{mi} \delta_{nj}, \quad (109b)$$

$$(\pi_T[\mathbf{E}_{\text{TE},mn}], \pi_T[\mathbf{E}_{\text{TM},ij}])_{\Gamma_{z^+}} = 0, \quad (109c)$$

where  $\delta$  denotes the Kronecker delta, the unknown coefficients  $\tilde{c}_{\alpha,mn} \in \mathbb{C}$  of the modal expansion (107) can be obtained as

$$\begin{aligned}\tilde{c}_{\alpha,mn} &= (\pi_T[\mathbf{E}], \pi_T[\mathbf{E}_{\alpha,mn}])_{\Gamma_{z^+}} \\ &= (\pi_T[\mathbf{E}^{\text{inc}}], \pi_T[\mathbf{E}_{\alpha,mn}])_{\Gamma_{z^+}} \\ &\quad + \underbrace{(\pi_T[\mathbf{E}^{\text{sc}}], \pi_T[\mathbf{E}_{\alpha,mn}])_{\Gamma_{z^+}}}_{=c_{\alpha,mn}}.\end{aligned} \quad (110)$$

Equation (107) represents the boundary condition to be imposed on  $\Gamma_{z^+}$ . In practice, the infinite sum of Floquet modes is truncated to  $-m_{\text{max}} \leq m \leq m_{\text{max}}, -n_{\text{max}} \leq n \leq n_{\text{max}}$ .

In that case we obtain a boundary condition in the form of (6e) with

$$\mathbf{F}^{\text{inc}} = 2Y^{\text{inc}} \pi_T[\mathbf{E}^{\text{inc}}], \quad (111)$$

$$\mathcal{G}(\mathbf{E}) = \sum_{\substack{|m| \leq m_{\text{max}} \\ |n| \leq n_{\text{max}} \\ \alpha \in \{\text{TE, TM}\}}} \tilde{c}_{\alpha,mn} Y_{\alpha,mn} \pi_T[\mathbf{E}_{\alpha,mn}], \quad (112)$$

Further simplifications are possible if the dimensions of the unit cell are small enough, such that only the fundamental modes  $\mathbf{E}_{\alpha,00}$  propagate, and the boundary  $\Gamma_{z^+}$  is placed sufficiently far away from the structure, such that all higher order modes are attenuated to a negligible amplitude. In this case, the fundamental mode is of particular interest and we may omit all evanescent higher order modes in (112). In particular, we can employ the first-order absorbing boundary condition [15, Chapter 13.4.1], i.e. (6e) with

$$\mathcal{G}(\mathbf{E}) = -\frac{\mathbf{k}_t^{\text{inc}}}{\omega\mu k_z^{\text{inc}}} (\mathbf{k}_t^{\text{inc}} \cdot \pi_T[\mathbf{E}]) - \frac{k_z^{\text{inc}}}{\omega\mu} \pi_T[\mathbf{E}], \quad (113)$$

where  $\mathbf{k}_t^{\text{inc}} := \pi_T[\mathbf{k}^{\text{inc}}]$ .

The corresponding terms in the boundary conditions of the dual problem (71) are given as

$$\bar{\mathcal{F}} = -\frac{j}{\omega\mu_0} \pi_T[\mathbf{E}_{\alpha,mn}], \quad (114)$$

and either

$$\bar{\mathcal{G}} = -\sum_{\alpha,m,n} \tilde{d}_{\alpha,mn}^* Y_{\alpha,mn}^* \pi_T[\mathbf{E}_{\alpha,mn}], \quad (115)$$

where  $\tilde{d}_{\alpha,mn} = (\pi_T[\mathbf{E}_{\alpha,mn}], \mathbf{z}_T)_{\Gamma_{z^+}}$ , if (112) is used for the primal problem, or

$$\bar{\mathcal{G}} = \frac{\mathbf{k}_t^{\text{inc}}}{\omega\mu_0 k_z^{\text{inc}}} (\mathbf{k}_t^{\text{inc}} \cdot \mathbf{z}_T) + \frac{k_z^{\text{inc}}}{\omega\mu_0} \mathbf{z}_T. \quad (116)$$

if lowest order Floquet boundary conditions (113) are employed in (6).

## B. Details on FE discretization

The mesh is assumed to be periodic, i.e. the surface meshes on  $\Gamma_{x^+}$  and  $\Gamma_{x^-}$ , as well as on  $\Gamma_{y^+}$  and  $\Gamma_{y^-}$ , are respectively identical. Without loss of generality we further

assume the vector of coefficients

$$\mathbf{c} = \begin{bmatrix} \mathbf{c}_{\text{inner}} \\ \mathbf{c}_{\Gamma_{z^+}} \\ \mathbf{c}_{\Gamma_{z^-}} \\ \mathbf{c}_{\Gamma_{x^+}} \\ \mathbf{c}_{\Gamma_{x^-}} \\ \mathbf{c}_{\Gamma_{y^+}} \\ \mathbf{c}_{\Gamma_{y^-}} \\ \mathbf{c}_{\Gamma_{x^+} \cap \Gamma_{y^+}} \\ \mathbf{c}_{\Gamma_{x^-} \cap \Gamma_{y^+}} \\ \mathbf{c}_{\Gamma_{x^+} \cap \Gamma_{y^-}} \\ \mathbf{c}_{\Gamma_{x^-} \cap \Gamma_{y^-}} \end{bmatrix} \in \mathbb{C}^{N_h} \quad (117)$$

to be ordered such that the boundary conditions imposed in (9) can be expressed as

$$\mathbf{c} = \underbrace{\begin{bmatrix} \mathbf{I} & 0 & 0 & 0 & 0 \\ 0 & \mathbf{I} & 0 & 0 & 0 \\ 0 & 0 & 0 & 0 & 0 \\ 0 & 0 & \mathbf{I} & 0 & 0 \\ 0 & 0 & \mathbf{I} e^{-j\psi_x} & 0 & 0 \\ 0 & 0 & 0 & \mathbf{I} & 0 \\ 0 & 0 & 0 & \mathbf{I} e^{-j\psi_y} & 0 \\ 0 & 0 & 0 & 0 & \mathbf{I} \\ 0 & 0 & 0 & 0 & \mathbf{I} e^{-j\psi_x} \\ 0 & 0 & 0 & 0 & \mathbf{I} e^{-j\psi_y} \\ 0 & 0 & 0 & 0 & \mathbf{I} e^{-j(\psi_x + \psi_y)} \end{bmatrix}}_{\mathbf{P}} \mathbf{c}_{\text{dof}}$$

where we have introduced the reduced vector

$$\mathbf{c}_{\text{dof}} = \begin{bmatrix} \mathbf{c}_{\text{inner}} \\ \mathbf{c}_{\Gamma_{z^+}} \\ \mathbf{c}_{\Gamma_{x^+}} \\ \mathbf{c}_{\Gamma_{y^+}} \\ \mathbf{c}_{\Gamma_{x^+} \cap \Gamma_{y^+}} \end{bmatrix} \in \mathbb{C}^{N_{\text{DoF}}} \quad (118)$$

of  $N_{\text{DoF}} < N_h$  DoF and  $\mathbf{I}$  denotes an identity matrix of appropriate size [15, Chapter 13.1.2].

Let  $\mathbf{A} \in \mathbb{C}^{N_h \times N_h}$  and  $\mathbf{f} \in \mathbb{C}^{N_h}$  be the system matrix and right-hand side vector, which are obtained by using (11) in (10), as well as Nédélec test functions. In case of using the higher-order Floquet port boundary condition, i.e. (6e) with (111), the boundary integrals lead to dense sub-blocks in the matrix  $\mathbf{A}$ , whereas (113) preserves the sparsity of the FE matrix. The quasi-periodic and PEC boundary conditions (9) on ansatz and test functions can be imposed conveniently using the matrix  $\mathbf{P} \in \mathbb{C}^{N_h \times N_{\text{DoF}}}$ , leading to the reduced system

$$\mathbf{A}_{\text{dof}} = \mathbf{P}^H \mathbf{A} \mathbf{P} \mathbf{c}_{\text{dof}} = \mathbf{P}^H \mathbf{f} = \mathbf{f}_{\text{dof}}, \quad (119)$$

where  $\mathbf{P}^H$  denotes the Hermitian transpose of  $\mathbf{P}$ . Functions spanned by the reduced DoF form a proper subspace of (9).

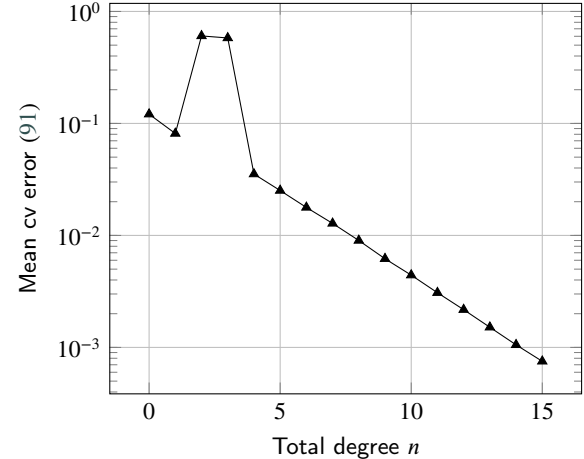


Figure 21: Convergence study of a gPC approximation using pseudo-spectral projection and sparse Gauss quadrature.

### C. Convergence study of gPC and sparse-grid projection

Since the computational cost for a proper convergence study in the 17-dimensional setting is too high, we restrict us again to the two most sensitive parameters, i.e.  $t_1, t_2$ , and repeat the gPC convergence study with sparse Gaussian quadrature. Again, we use a random cross-validation sample of size  $N^{\text{MC}} = 1000$  to compute the error (91). Results are presented in Fig. 21. It can be observed that, similar to Fig. 17, the error slightly increases up to order 3 before a convergent behavior can indeed be observed.

## References

- [1] C. Genet and T. W. Ebbesen. Light in tiny holes. *Nature*, 445:39, 2007. doi:<http://dx.doi.org/10.1038/nature05350>
- [2] S. A. Maier. *Plasmonics: fundamentals and applications*. Springer Science & Business Media, New York, 2007.
- [3] B. S. Dennis *et al.* Enhanced coupling between light and surface plasmons by nano-structured fabry–perot resonator. *J. Appl. Phys.*, 110:066102, 2011.
- [4] J. Lu *et al.* Numerical optimization of a grating coupler for the efficient excitation of surface plasmons at an Ag–SiO<sub>2</sub> interface. *J. Opt. Soc. Am. B*, 24:2268, 2007.
- [5] M. J. Preiner *et al.* Efficient optical coupling into metal-insulator-metal plasmon modes with subwavelength diffraction gratings. *Appl. Phys. Lett.*, 92(11):113109, 2008. doi:[10.1063/1.2898509](https://doi.org/10.1063/1.2898509).
- [6] B. Gallinet, J. Butet, and O. J. Martin. Numerical methods for nanophotonics: standard problems and future challenges. *Laser Photonics Rev.*, 9(6):577–603, 2015.
- [7] P. Lalanne and G. M. Morris. Highly improved convergence of the coupled-wave method for TM polarization. *J. Opt. Soc. Am. A*, 13(4):779–784, 1996.
- [8] G. Granet and B. Guizal. Efficient implementation of the coupled-wave method for metallic lamellar gratings in TM polarization. *J. Opt. Soc. Am. A*, 13(5):1019–1023, 1996.
- [9] K. S. Kunz and R. J. Luebbers. *The finite difference time domain method for electromagnetics*. CRC press, Boca Raton, 1993.
- [10] T. Weiland. Time domain electromagnetic field computation with finite difference methods. *Int. J. Numer. Model. Electron. Netw.*

work. *Dev. Field*, 9(4):295–319, 1996. doi:10.1002/(SICI)1099-1204(199607)9:4<295::AID-JNM240>3.0.CO;2-8.

[11] A. Tafove and S. C. Hagness. *Computational electrodynamics: the finite-difference time-domain method*. Artech house, Norwood, 2005.

[12] F. G. De Abajo and J. Aizpurua. Numerical simulation of electron energy loss near inhomogeneous dielectrics. *Phys. Rev. B*, 56(24):15873, 1997.

[13] J. Waxenegger, A. Trügler, and U. Hohenester. Plasmonics simulations with the MNPBEM toolbox: Consideration of substrates and layer structures. *Comput. Phys. Commun.*, 193:138–150, 2015.

[14] G. Unger, A. Trügler, and U. Hohenester. Novel modal approximation scheme for plasmonic transmission problems. *Phys. Rev. Lett.*, 121:246802, 2018. doi:10.1103/PhysRevLett.121.246802.

[15] J.-M. Jin. *The Finite Element Method in Electromagnetics*. John Wiley & Sons, Hoboken, 2015.

[16] P. Monk. *Finite element methods for Maxwell's equations*. Oxford University Press, 2003.

[17] C. Chauviere, J. S. Hesthaven, and L. Lurati. Computational modeling of uncertainty in time-domain electromagnetics. *SIAM J. Sci. Comput.*, 28(2):751–775, 2006.

[18] J. Niegemann *et al.* Higher-order time-domain methods for the analysis of nano-photonic systems. *Photonics Nanostructures: Fundam. Appl.*, 7(1):2–11, 2009.

[19] K. Busch, M. König, and J. Niegemann. Discontinuous Galerkin methods in nanophotonics. *Laser Photonics Rev.*, 5(6):773–809, 2011.

[20] N. Schmitt *et al.* A DGTD method for the numerical modeling of the interaction of light with nanometer scale metallic structures taking into account non-local dispersion effects. *J. Comput. Phys.*, 316:396–415, 2016.

[21] N. Schmitt *et al.* Simulation of three-dimensional nanoscale light interaction with spatially dispersive metals using a high order curvilinear DGTD method. *J. Comput. Phys.*, 2018.

[22] D. Xiu. Fast numerical methods for stochastic computations: A review. *Commun. Comput. Phys.*, 5(2-4):242–272, 2009.

[23] R. G. Ghanem and P. D. Spanos. *Stochastic Finite Elements: A Spectral Approach*. Springer, New York, 1991.

[24] I. Babuska, R. Tempone, and G. E. Zouraris. Galerkin finite element approximations of stochastic elliptic partial differential equations. *SIAM J. Numer. Anal.*, 42(2):800–825, 2004.

[25] I. Babuska, F. Nobile, and R. Tempone. A stochastic collocation method for elliptic partial differential equations with random input data. *SIAM Review*, 2:317–355, 2010.

[26] D. Xiu and G. E. Karniadakis. The Wiener-Askey polynomial chaos for stochastic differential equations. *SIAM J. Sci. Comput.*, 24(2):619–644, 2002.

[27] D. Xiu and J. S. Hesthaven. High-order collocation methods for differential equations with random inputs. *SIAM J. Sci. Comput.*, 27(3):1118–1139, 2005.

[28] A. Chkifa, A. Cohen, and C. Schwab. High-dimensional adaptive sparse polynomial interpolation and applications to parametric pdes. *Found. Comput. Math.*, 14(4):601–633, 2014.

[29] T. Gerstner and M. Griebel. Dimension-adaptive tensor-product quadrature. *Computing*, 71(1):65–87, 2003.

[30] A. Narayan and J. D. Jakeman. Adaptive Leja sparse grid constructions for stochastic collocation and high-dimensional approximation. *SIAM J. Sci. Comput.*, 36(6), 2014.

[31] F. Nobile, R. Tempone, and C. G. Webster. An anisotropic sparse grid stochastic collocation method for partial differential equations with random input data. *SIAM J. Numer. Anal.*, 46(5):2411–2442, 2008.

[32] O. G. Ernst, B. Sprungk, and L. Tamellini. Convergence of sparse collocation for functions of countably many gaussian random variables (with application to elliptic PDEs). *SIAM J. Numer. Anal.*, 56(2):877–905, 2018.

[33] O. P. Le Maître and O. M. Knio. *Spectral Methods for Uncertainty Quantification: With Applications to Computational Fluid Dynamics*. Scientific Computation. Springer Netherlands, 2010.

[34] P. Sochala and O. P. Le Maître. Polynomial chaos expansion for subsurface flows with uncertain soil parameters. *Adv. Water Resour.*, 62:139 – 154, 2013. doi:<https://doi.org/10.1016/j.advwatres.2013.10.003>.

[35] G. Blatman and B. Sudret. An adaptive algorithm to build up sparse polynomial chaos expansions for stochastic finite element analysis. *Probabilistic Engineering Mechanics*, 25(2):183 – 197, 2010. doi:<https://doi.org/10.1016/j.probengmech.2009.10.003>.

[36] M. Motamed, F. Nobile, and R. Tempone. A stochastic collocation method for the second order wave equation with a discontinuous random speed. *Numerische Mathematik*, 123(3):493–536, 2013.

[37] A. C. M. Austin and C. D. Sarris. Efficient analysis of geometrical uncertainty in the FDTD method using polynomial chaos with application to microwave circuits. *IEEE Trans. Microw. Theory Tech.*, 61(12):4293–4301, 2013. doi:10.1109/TMTT.2013.2281777.

[38] N. Georg *et al.* Uncertainty quantification for Maxwell's eigenproblem using isogeometric analysis and mode tracking. *Comput. Meth. Appl. Mech. Eng.*, 350:228–244, 2019. arXiv: 1802.02978.

[39] D. Loukrezis, U. Römer, and H. De Gersem. Assessing the performance of Leja and Clenshaw-Curtis collocation for computational electromagnetics with random input data. *Int. J. for Uncertain. Quantif.*, 9(1):33–57, 2019.

[40] R. Hiptmair *et al.* Large deformation shape uncertainty quantification in acoustic scattering. *Adv. Comput. Math.*, pages 1–44, 2018.

[41] L. Scarabosio. *Shape uncertainty quantification for scattering transmission problems*. PhD thesis, ETH Zurich, 2016.

[42] T. Wittig, R. Schuhmann, and T. Weiland. Model order reduction for large systems in computational electromagnetics. *Linear Algebra Appl.*, 415(2-3):499–530, 2006.

[43] P. Benner and J. Schneider. Uncertainty quantification for Maxwell's equations using stochastic collocation and model order reduction. *Int. J. Uncertain. Quantif.*, 5(3), 2015.

[44] O. Farle *et al.* Multivariate finite element model order reduction for permittivity or permeability estimation. *IEEE Trans. Magn.*, 42(4):623–626, 2006.

[45] P. Benner, S. Gugercin, and K. Willcox. A survey of projection-based model reduction methods for parametric dynamical systems. *SIAM review*, 57(4):483–531, 2015.

[46] A. Bodendiek and M. Bollhöfer. Adaptive-order rational arnoldi-type methods in computational electromagnetism. *BIT Numerical Mathematics*, 54(2):357–380, 2014.

[47] F. Bonizzoni *et al.* Least-Squares Padé approximation of parametric and stochastic Helmholtz maps. *ArXiv e-prints*, 2018.

[48] T. Chantrasmi, A. Doostan, and G. Iaccarino. Padé–Legendre approximants for uncertainty analysis with discontinuous response surfaces. *J. Comput. Phys.*, 228(19):7159–7180, 2009.

[49] G. Silva-Oelker *et al.* Quantifying the impact of random surface perturbations on reflective gratings. *IEEE Trans. Antennas Propag.*, 66(2):838–847, 2017.

[50] P. Jantsch and C. Webster. Sparse grid quadrature rules based on conformal mappings. In *Sparse Grids and Applications-Miami 2016*, pages 117–134. Springer, 2018.

[51] L. N. Trefethen. *Approximation theory and approximation practice*, volume 128. SIAM, 2013.

[52] T. Butler, P. Constantine, and T. Wildey. A posteriori error analysis of parameterized linear systems using spectral methods. *SIAM J. Matrix Anal. Appl.*, 33(1):195–209, 2012.

[53] T. Butler, C. Dawson, and T. Wildey. Propagation of uncertainties using improved surrogate models. *SIAM/ASA J. Uncertain.*, 1(1):164–191, 2013.

[54] J. D. Jakeman and T. Wildey. Enhancing adaptive sparse grid approximations and improving refinement strategies using adjoint-based a posteriori error estimates. *J. Comput. Phys.*, 280:54–71, 2015.

[55] B. Schieche. *Unsteady Adaptive Stochastic Collocation on Sparse Grids*. PhD Thesis, TU Darmstadt, 2012.

[56] D. Loukrezis and H. De Gersem. Approximation and uncertainty quantification of stochastic systems with arbitrary input distributions using weighted Leja interpolation. *arXiv e-prints*, page arXiv:1904.07709, 2019.

[57] I.-G. Farcas *et al.* Multilevel adaptive sparse Leja approximations for Bayesian inverse problems. *arXiv e-prints*, page arXiv:1904.12204, 2019.

[58] A. Pitelet *et al.* Influence of spatial dispersion on surface plasmons, nanoparticles and grating couplers. *arXiv e-prints*, page arXiv:1904.01456, 2019.

[59] N. Schmitt *et al.* Optimization and uncertainty quantification of gradient index metasurfaces. *Opt. Mater. Express*, 9(2):892–910, 2019. doi:10.1364/OME.9.000892.

[60] J. C. Nedelec. Mixed finite elements in  $R^3$ . *Numer. Math.*, 35(3):315–341, 1980. doi:10.1007/BF01396415.

[61] R. Jankoski, U. Römer, and S. Schöps. Stochastic modeling of magnetic hysteretic properties by using multivariate random fields. *Int. J. Uncertain. Quantif.*, 9(1), 2019.

[62] R. Lebrun and A. Dutfoy. Do Rosenblatt and Nataf isoprobabilistic transformations really differ? *Probabilist. Eng. Mech.*, 24(4):577–584, 2009.

[63] D. Xiu. *Numerical Methods for Stochastic Computations: A Spectral Method Approach*. Princeton University Press, Princeton, 2010.

[64] G. Blatman and B. Sudret. Adaptive sparse polynomial chaos expansion based on least angle regression. *J. Comput. Phys.*, 230(6):2345–2367, 2011.

[65] B. J. Debusschere *et al.* Numerical challenges in the use of polynomial chaos representations for stochastic processes. *SIAM J. Sci. Comput.*, 26(2):698–719, 2004.

[66] O. P. Le Maître *et al.* A stochastic projection method for fluid flow: I. basic formulation. *J. Comput. Phys.*, 173(2):481–511, 2001.

[67] G. Migliorati *et al.* Analysis of discrete L2 projection on polynomial spaces with random evaluations. *Found. Comput. Math.*, 14(3):419–456, 2014.

[68] V. Barthelmann, E. Novak, and K. Ritter. High dimensional polynomial interpolation on sparse grids. *Adv. Comput. Math.*, 12(4):273–288, 2000.

[69] H.-J. Bungartz and M. Griebel. Sparse grids. *Acta Numerica*, 13:147–269, 2004. doi:10.1017/S0962492904000182.

[70] A. Klimke and B. I. Wohlmuth. Algorithm 847: Spinterp: Piecewise multilinear hierarchical sparse grid interpolation in MATLAB. *ACM Trans. Math. Softw.*, 31(4):561–579, 2005.

[71] F. Nobile, R. Tempone, and C. G. Webster. A sparse grid stochastic collocation method for partial differential equations with random input data. *SIAM J. Numer. Anal.*, 46(5):2309–2345, 2008.

[72] N. Hale and L. N. Trefethen. New quadrature formulas from conformal maps. *SIAM J. Numer. Anal.*, 46(2):930–948, 2008.

[73] N. Hale. *On the use of conformal maps to speed up numerical computations*. PhD thesis, Oxford University, 2009.

[74] D. Kosloff and H. Tal-Ezer. A modified Chebyshev pseudospectral method with an  $\mathcal{O}(N - 1)$  time step restriction. *J. Comput. Phys.*, 104(2):457–469, 1993.

[75] J. Bertrut and L. Trefethen. Barycentric Lagrange interpolation. *SIAM Review*, 46(3):501–517, 2004.

[76] S. A. Smolyak. Quadrature and interpolation formulas for tensor products of certain classes of functions. *Dokl. Acad. Nauk SSSR*, 4:240–243, 1963.

[77] R. Becker and R. Rannacher. An optimal control approach to a posteriori error estimation in finite element methods. *Acta Numerica*, 10:1–102, 2001.

[78] U. Römer and S. Schöps. Adjoint error estimation for a pseudospectral approach to stochastic field-circuit coupled problems. In *Proc. Appl. Math. Mech.*, volume 15, Wiley-VCH, pages 711–714, 2015. doi:10.1002/pamm.201510345.

[79] A. L. Teckentrup *et al.* Further analysis of multilevel Monte Carlo methods for elliptic PDEs with random coefficients. *Numer. Math.*, 125(3):569–600, 2013. doi:10.1007/s00211-013-0546-4.

[80] CST AG. Optical applications with CST Microwave Studio, 2012. [https://www.cst.com/content/events/downloads/euc2012/talk\\_5-3-1\\_cst\\_euc\\_2012.pdf](https://www.cst.com/content/events/downloads/euc2012/talk_5-3-1_cst_euc_2012.pdf) (Accessed: 2018-03-12).

[81] P. B. Johnson and R.-W. Christy. Optical constants of the noble metals. *Physical review B*, 6(12):4370, 1972.

[82] C. Geuzaine and J.-F. Remacle. Gmsh: A 3-D finite element mesh generator with built-in pre-and post-processing facilities. *Int. J. Numer. Meth. Eng.*, 79(11):1309–1331, 2009.

[83] M. Alnæs *et al.* The FEniCS project version 1.5. *Archive of Numerical Software*, 3(100):9–23, 2015.

[84] CST AG. CST STUDIO SUITE 2016, 2018.

[85] V. Braibant and C. Fleury. Shape optimal design using B-splines. *Comput. Methods Appl. Mech. Eng.*, 44(3):247–267, 1984. doi:10.1016/0045-7825(84)90132-4.

[86] L. Piegl and W. Tiller. *The NURBS Book*. Springer, 2 edition, 1997.

[87] J. Nocedal and S. J. Wright. *Numerical optimization*. Springer Series in Operations Research and Financial Engineering. Springer, New York, 2nd edition, 2006.

[88] R. H. Lopes. Kolmogorov-Smirnov test. In *International Encyclopedia of Statistical Science*, pages 718–720. Springer, 2011.

[89] F. Nobile and R. Tempone. Analysis and implementation issues for the numerical approximation of parabolic equations with random coefficients. *Int. J. Numer. Meth. Eng.*, 80(6-7):979–1006, 2009.

[90] J. Feinberg and H. P. Langtangen. Chaospy: An open source tool for designing methods of uncertainty quantification. *J. Comput. Science*, 11:46–57, 2015.

[91] D. Loukrezis. Dimension Adaptive Leja Interpolation (DALI), 2018.

[92] J. Li and D. Xiu. Evaluation of failure probability via surrogate models. *J. Comput. Phys.*, 229(23):8966–8980, 2010. doi:10.1016/j.jcp.2010.08.022.

[93] V. A. Epanetnikov. Non-parametric estimation of a multivariate probability density. *Theor. Probab. Appl.*, 14(1):153–158, 1969.

[94] I. M. Sobol. Global sensitivity indices for nonlinear mathematical models and their Monte Carlo estimates. *Math. Comput. Simul.*, 55(1):271 – 280, 2001. doi:[https://doi.org/10.1016/S0378-4754\(00\)00270-6](https://doi.org/10.1016/S0378-4754(00)00270-6).

[95] T. Homma and A. Saltelli. Importance measures in global sensitivity analysis of nonlinear models. *Reliab. Eng. Syst. Safe.*, 52(1):1–17, 1996.

[96] A. Saltelli. Making best use of model evaluations to compute sensitivity indices. *Comput. Phys. Commun.*, 145(2):280–297, 2002.

[97] J. Bäck *et al.* Stochastic spectral Galerkin and collocation methods for PDEs with random coefficients: a numerical comparison. In J. Hesthaven and E. Ronquist, editors, *Spectral and High Order Methods for Partial Differential Equations*, volume 76 of *Lecture Notes in Computational Science and Engineering*, pages 43–62. Springer, 2011. Selected papers from the ICOSAHOM '09 conference, June 22–26, Trondheim, Norway.

[98] A. K. Bhattacharyya. *Phased array antennas: Floquet analysis, synthesis, BFNs and active array systems*, volume 179. John Wiley & Sons, Hoboken, 2006.

[99] Y. Zhu and A. C. Cangellaris. *Multigrid finite element methods for electromagnetic field modeling*, volume 28. John Wiley & Sons, Hoboken, 2006.